Statistical Analysis of Cavity Quality Factor Due to Localized Losses With the Stochastic Green's Function Method

Shen Lin, *Member, IEEE*, Sangrui Luo, *Student Member, IEEE*, Yang Shao, *Member, IEEE*, Bisrat D. Addissie, Zachary B. Drikas, *Member, IEEE*, Gabriele Gradoni, *Member, IEEE*, and Zhen Peng, *Senior Member, IEEE*

***Abstract*—The statistical characterization of the cavity quality factor (Q-factor) holds significant practical importance, especially in the context of large and complex metallic enclosures. While there are existing methods for analyzing Q-factor statistics attributed to distributed and uniform losses, there is a noticeable gap in addressing the statistical cavity Q-factor arising from localized losses, such as aperture leakage, wall coating, and absorptive loading. This article introduces a physics-oriented, hybrid deterministic-stochastic approach to predict the statistical distribution of cavity Q-factor due to localized losses. The key ingredient of this method is the stochastic Green's function integral equation formulation, grounded in a statistical description of the cavity eigenmodes within an enclosed electromagnetic environment. The computational model is evaluated through both numerical and laboratory experiments, validating its reliability and applicability in real-world scenarios.**

***Index Terms*—Chaos, Green function, mode-stirred reverberation chambers (MSRCs), quality factor (Q-factor), statistical analysis.**

I. Introduction

IN CONFINED electromagnetic (EM) environments, the quality factor (Q-factor) is an essential parameter to characterize the energy loss inside the cavity, and also a key quality in understanding and analyzing the properties of internal EM fields. Applications include electromagnetic compatibility (EMC) testing in mode-stirred reverberation chambers (MSRCs) [1], [2], [3], [4], [5], the study of intentional electromagnetic interference (EMI) to electronics housed inside metallic enclosures [6], [7], [8], [9], [10], [11], [12], and the analysis of channel properties (coherent bandwidth, spatial correlation, power decay profile) in the indoor wireless over-the-air (OTA) testing [13], [14], [15], [16].

Historically in the study of cavity resonators, the modal Q-factor was introduced as a measure to account for dielectric and wall losses inside the cavity for a single eigenmode. This parameter, defined by the ratio of stored energy to dissipated power, multiplied by the modal frequency [17], [18], laid the groundwork for understanding power and energy behavior within these resonators. However, the modal Q-factor becomes less effective in analyzing the high-frequency reverberation, as the complex boundary of the enclosure can lead to high modal density and high modal overlap. As a result, the literature introduced the composite, effective Q-factor as an average value (frequency-averaged or stir-averaged) of the cavity Q-factor [19], [20]. It is noted that the composite Q-factor typically varies smoothly with operating frequency. It does not characterize the quasi-random fluctuations between nearby frequencies or different cavity configurations. This limitation underscores the need for characterizing the cavity Q-factor in terms of a statistical measure, such as the probability density function (PDF).

Broadly speaking, the losses inside a realistic cavity can be characterized into two categories. One refers to homogeneous, distributed losses throughout the cavity surface and volume, e.g., wall loss due to the power dissipated in the metal walls and material loss from power absorbed in the dielectric materials uniformly filled in the cavity. For those distributed losses, it is predicted that the PDF of Q-factor exhibits a Fisher–Snedecor F-distribution [21], [22], [23], assuming statistically homogeneous and isotropic cavity fields. The theoretical prediction is verified experimentally in the MSRC setting. Another noticeable work utilizing the volumetric number of independent field samples and the central limit theorem is presented in [24], [25], and [26], which concludes that the Q-factor PDF is basically normal distribution in the overmoded regime of well-stirred reverberation chambers.

While existing research has primarily focused on the Q-factor statistics for cavities with homogeneous, distributed losses, there has been little discussion of the statistical cavity Q-factor due

Manuscript received 2 January 2024; revised 21 February 2024; accepted 9 March 2024. Date of publication 9 April 2024; date of current version 13 June 2024. This work was supported in part by the U.S. National Science Foundation (NSF) CAREER Award, #1750839, in part by the U.S. Office of Naval Research (ONR) Award #N00014-20-1-2835, ONR Award #N0001423WX00051, and in part by the U.S. Defense Advanced Research Projects Agency (DARPA) Award #HR0011-21-2-00211. *(Corresponding author: Zhen Peng.)*

Shen Lin, Sangrui Luo, Yang Shao, and Zhen Peng are with the Center for Computational Electromagnetics, Department of Electrical and Computer Engineering, University of Illinois at Urbana-Champaign, Urbana, IL 61801 USA (e-mail: shenlin2@illinois.edu; sangrui2@illinois.edu; yangshao@illinois.edu; zvpeng@illinois.edu).

Bisrat D. Addissie and Zachary B. Drikas are with U.S. Naval Research Laboratory, Washington, DC 20375 USA (e-mail: bisrat.addissie@nrl.navy.mil; zachary.drikas@nrl.navy.mil).

Gabriele Gradoni is with the Department of Electrical and Electronic Engineering, University of Surrey, GU2 7XH Guildford, U.K., and also with the Department of Electrical and Computer Engineering, University of Illinois at Urbana-Champaign, Urbana, IL 61801 USA (e-mail: g.gradoni@surrey.ac.uk).

Color versions of one or more figures in this article are available at https://doi.org/10.1109/TEMC.2024.3380189.

Digital Object Identifier 10.1109/TEMC.2024.3380189

to localized losses (e.g., aperture leakage, absorptive loading). Unlike the case of homogeneous losses, localized losses depend on the specific lossy components involved. Taking the aperture leakage as an example, the power loss through the aperture depends on the aperture shape, surface area, and operating frequency of interest. Therefore, it becomes necessary to integrate these component-specific attributes into the statistical Q-factor prediction.

The contribution of this work is a hybrid deterministic-stochastic model that is built upon a recently developed stochastic Green's function (SGF) method [27], [28], [29]. The SGF can be considered as a physics-oriented, statistical surrogate model for the vector wave equation in large, complex enclosures. It provides a computationally efficient approximation of enclosed EM environments based on a statistical representation of the cavity eigenfunctions and eigenvalues. By leveraging the SGF method as a cavity surrogate model, we integrate the component-specific features of the localized losses through an SGF surface integral equation (IE) formulation. The statistical predictions of aperture leakage, absorptive loading, and wall coating are validated by numerical simulations and experimental results. To the best of authors' knowledge, the work represents an original contribution and the first result to analyze the statistical Q-factor for localized losses in the literature.

We remark that the initial study of this work has been reported in a conference paper [30]. This article significantly extends and elaborates the approaches and numerical experiments presented in [30].

II. Methodology for Absorptive Loading

A. Background and Problem Statement

The Q-factor of the enclosure is a key quality in calculating the statistical properties of internal EM fields in an electrically large cavity. Generally, the Q-factor Q is defined as

$$Q(\omega) = \omega \frac{U_s(\omega)}{P_d(\omega)} \tag{1}$$

where ω is the angular frequency, U_s is the steady-state energy stored in the cavity, and P_d is the dissipated power. It is noted that the macroscopic definition of Q-factor as in [21], [24], and [23] is considered here, instead of modal Q-factors for individual cavity eigenmodes. We are interested in studying the fluctuation of the Q-factor for an ensemble of statistically similar cavity environments, i.e., varying stir states in an MSRC, or changing the frequency within the coherence bandwidth.

Broadly speaking, the statistical fluctuation of the Q-factor depends on the nature of the loss mechanisms contributing to the dissipated power P_d. If the loss is distributed throughout the enclosure, the fluctuations in Q-factor are small. This was an assertion that was tested early in the development of what is known as "wave chaos" [31]. However, if the loss is localized in the cavity, the Q-factor can fluctuate significantly, which is the primary interest of this article.

Consider an electrically large, complex cavity with both uniform distributed losses and localized losses, the Q-factor can be expressed as

$$\begin{aligned} Q^{-1}(\omega) &= Q_{\text{uni}}^{-1}(\omega) + Q_{\text{loc}}^{-1}(\omega) \\ &= \frac{1}{\omega}\frac{P_{d,\text{uni}}(\omega)}{U_s(\omega)} + \frac{1}{\omega}\frac{P_{d,\text{loc}}(\omega)}{U_s(\omega)}. \end{aligned} \tag{2}$$

In the following, we will analyze the statistical Q-factor, denoted as Q_{loc}, attributed to three distinct localized loss mechanisms: absorptive loading (discussed in this section), aperture leakage, and wall coating (covered in Section III).

Taking the case of dielectric loading as an example, the design of the numerical experiment is illustrated in Fig. 1. Here, a small electric dipole is placed inside the cavity as the transmitter (Tx). This Tx dipole is responsible for the cavity excitation. The other sets of receiving (Rx) electric dipoles are utilized as the probe devices to measure the received vectorial electric fields (E-fields), denoted as $\mathrm{E^x}$, $\mathrm{E^y}$, and $\mathrm{E^z}$.

Next, we introduce an artificial surface S_{d} over the boundary of the dielectric object to facilitate the calculation of surface electric and magnetic currents. By leveraging the data collected from the internal E-fields and surface currents, we can obtain the stored energy U_s within the cavity and the dissipated power $P_{d,\text{loc}}$ in the dielectric loading. The ratio between ωU_s and $P_{d,\text{loc}}$ gives rise to the Q_{loc}, according to (2).

To acquire a statistical ensemble of cavity Q-factor Q_{loc}, one may rotate the mode stirrer in numerical experiment and collect the U_s and $P_{d,\text{loc}}$ for each stirrer state. It is clear that when first-principles numerical modeling is used, we need many full-wave simulations to obtain a statistical ensemble of U_s and $P_{d,\text{loc}}$. The computation complexity is prohibitively expensive for electrically large cavities. In this work, we address this challenge by harnessing the capabilities of a recently developed statistical wave model known as the stochastic dyadic Green's function (S-DGF). This model serves as an efficient and effective statistical solution to the vector wave equation within large

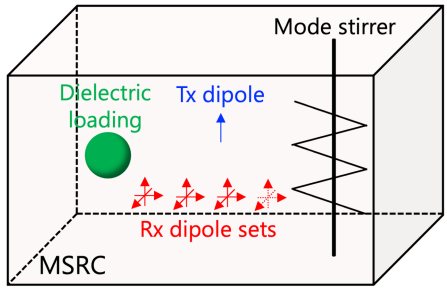

Fig. 1. Illustration of the design of the numerical experiment for dielectric loading.

TABLE I
Quantitative Measure of the Statistical Prediction

Methods	Mean value		KL divergence	
	Cube	Sphere	Cube	Sphere
RPW	2201.69	4015.17	N.A.	N.A.
Full-wave	2169.58	3818.86		
Proposed work ($\alpha = 0.1$)	2015.06	3713.79	0.0753	0.0193
Proposed work ($\alpha = 1$)	2035.10	3764.69	0.1094	0.0165
Proposed work ($\alpha = 10$)	2050.85	3809.20	0.1120	0.0175

and complex enclosures. The utilization of S-DGF significantly enhances the computational efficiency of our numerical analysis.

B. Introduction of S-DGF

The S-DGF is based on a statistical description of the eigenmodes of an enclosed EM environment. Let us consider a 3-D metallic cavity of volume V featuring distributed losses. The cavity wall is modeled as a perfect electric conductor (PEC) boundary condition. Within the cavity, the volume is filled with a homogeneous medium characterized by permittivity ϵ_0, permeability μ_0, and conductivity σ. It is noted that the medium conductivity σ is introduced to account for the homogeneous, distributed losses occurring within the cavity.

Consider the second-order vector wave equation

$$\nabla \times \nabla \times \mathbf{E}(\mathbf{r}) - \tilde{k}^2 \mathbf{E}(\mathbf{r}) = -j\omega\mu_0 \mathbf{J}(\mathbf{r}') \tag{3}$$

where $\tilde{k}^2$ is the square of complex wave number, defined by

$$\tilde{k}^2 = \omega^2 \mu_0 \epsilon_0 - j\omega\mu_0\sigma = k^2 - jk^2/Q_{\text{uni}} \tag{4}$$

in which $k = \omega\sqrt{\mu_0\epsilon_0}$ is the free-space wavenumber, and the cavity Q-factor $Q_{\text{uni}} = \omega\epsilon_0/\sigma$.

The electric dyadic Green's function satisfies

$$\nabla \times \nabla \times \overline{\mathbf{G}}^{\text{ee}}(\mathbf{r}, \mathbf{r}') - \tilde{k}^2 \overline{\mathbf{G}}^{\text{ee}}(\mathbf{r}, \mathbf{r}') = -\bar{\mathbf{I}}\delta(\mathbf{r} - \mathbf{r}') \tag{5}$$

where $\bar{\mathbf{I}}$ is the unit dyad (idemfactor) and superscript ee identifies the contribution from the electric current source to the E-field.

The stochastic DGF in the dyadic form can be constructed through the expansion of eigenfunctions [29, Appendix A]

$$\overline{\mathbf{G}}_{\text{S}}^{\text{ee}}(\mathbf{r}, \mathbf{r}') = \sum_i \frac{\boldsymbol{\Psi}_i^{\text{e}}(\mathbf{r}, k_i) \otimes \boldsymbol{\Psi}_i^{\text{e}}(\mathbf{r}', k_i)}{k^2 - k_i^2 - j\frac{k^2}{Q_{\text{uni}}}} \tag{6}$$

where $\otimes$ indicates an outer product between two vectors. $\boldsymbol{\Psi}_i^{\text{e}}$ and k_i are the ith electric eigenvector and eigenvalue of the cavity. In prior work, we proposed the substitution of approximate, statistically defined eigenvectors and eigenvalues. Specifically, the statistics of eigenvectors are derived from Berry's random wave model (RWM) [32], taking into account different orientations of polarization. The statistics for eigenvalues are generated using Wigner's random matrix theory (RMT) [33].

After incorporating the RWM and RMT approximation, the expression of S-DGF for a pair of source and field points is given by [29]

$$\overline{\mathbf{G}}_{\text{S}}^{\text{ee}}(\mathbf{r}, \mathbf{r}') = \text{Re}\left[\overline{\mathbf{G}}_0^{\text{ee}}(\mathbf{r}, \mathbf{r}')\right] + \sum_m \frac{\overline{\mathbf{D}}_{\text{S}}^{\text{ee}}(\mathbf{r}, \mathbf{r}'; k_m)}{\tilde{\lambda}_m - j\alpha} \frac{kV}{2\pi^2} \tag{7}$$

where $\overline{\mathbf{G}}_0^{\text{ee}}(\mathbf{r}, \mathbf{r}')$ is the electric dyadic Green's function of free-space. $\overline{\mathbf{D}}_{\text{S}}^{\text{ee}}(\mathbf{r}, \mathbf{r}'; k_m)$ is a dyadic product of correlated Gaussian random variables. We have shown that the mean value of $\overline{\mathbf{D}}_{\text{S}}^{\text{ee}}(\mathbf{r}, \mathbf{r}'; k_m)$ is related to the homogeneous Green's dyadic as

$$\left\langle \overline{\mathbf{D}}_{\text{S}}^{\text{ee}}(\mathbf{r}, \mathbf{r}'; k_m) \right\rangle = -\frac{2\pi}{k_m V} \text{Im}\left[\overline{\mathbf{G}}_0^{\text{ee}}(\mathbf{r}, \mathbf{r}')\right]. \tag{8}$$

The eigenvalues $\tilde{\lambda}$ are calculated from the Gaussian orthogonal ensemble (GOE) of random matrices, and α is a macroscopic dimensionless loss-parameter defined by $\alpha = k^3 V/(2\pi^2 Q_{\text{uni}})$.

C. Extension of S-DGF

In order to conduct surface IE-based modeling of the dielectric object, it is imperative to extend the S-DGF of electric type to general forms of Green's dyadic. These dyadics characterize the contributions from the magnetic current source to the magnetic field ($\overline{\mathbf{G}}_{\text{S}}^{\text{mm}}$), from the electric current source to the magnetic field ($\overline{\mathbf{G}}_{\text{S}}^{\text{me}}$), and from the magnetic current source to the E-field ($\overline{\mathbf{G}}_{\text{S}}^{\text{em}}$).

Consider the second-order vector wave equation

$$\nabla \times \nabla \times \mathbf{H}(\mathbf{r}) - \tilde{k}^2 \mathbf{H}(\mathbf{r}) = -j\omega\epsilon \mathbf{M}(\mathbf{r}'). \tag{9}$$

The magnetic dyadic Green's function satisfies

$$\nabla \times \nabla \times \overline{\mathbf{G}}^{\text{mm}}(\mathbf{r}, \mathbf{r}') - \tilde{k}^2 \overline{\mathbf{G}}^{\text{mm}}(\mathbf{r}, \mathbf{r}') = -\bar{\mathbf{I}}\delta(\mathbf{r} - \mathbf{r}'). \tag{10}$$

It is easy to show that a similar eigenfunction expansion exists for $\overline{\mathbf{G}}^{\text{mm}}$, denoted by

$$\overline{\mathbf{G}}_{\text{S}}^{\text{mm}}(\mathbf{r}, \mathbf{r}') = \sum_i \frac{\boldsymbol{\Psi}_i^{\text{m}}(\mathbf{r}, k_i) \otimes \boldsymbol{\Psi}_i^{\text{m}}(\mathbf{r}', k_i)}{k^2 - k_i^2 - j\frac{k^2}{Q_{\text{uni}}}} \tag{11}$$

where $\boldsymbol{\Psi}_i^{\text{m}}$ is the ith magnetic eigenvector of the cavity. In a cavity resonator, these magnetic eigenvectors can be constructed from the electric eigenvectors by the relation $k_i \boldsymbol{\Psi}_i^{\text{m}} = \nabla \times \boldsymbol{\Psi}_i^{\text{e}}$ [34].

We recall that after incorporating the RWM, the vector components of $\boldsymbol{\Psi}_i^{\text{e}}$ are expressed as a superposition of many plane waves with uniformly distributed orientation and polarization. In the Cartesian coordinate system, we have

$$\boldsymbol{\Psi}_i^{\text{e}}(\mathbf{r}, k_i) = \Psi_i^{\text{e},x}(\mathbf{r})\,\hat{\mathbf{x}} + \Psi_i^{\text{e},y}(\mathbf{r})\,\hat{\mathbf{y}} + \Psi_i^{\text{e},z}(\mathbf{r})\,\hat{\mathbf{z}} \tag{12}$$

where the vector components are

$$\Psi_i^{\text{e},x}(\mathbf{r}) \simeq \lim_{N\to\infty} \sum_{n=1}^{N} [a_n(-\cos\psi_n \sin\phi_n - \sin\psi_n \cos\phi_n \cos\theta_n) \cos(k_i \hat{\mathbf{e}}_n \cdot \mathbf{r} + \beta_n)] \tag{13}$$

$$\Psi_i^{\text{e},y}(\mathbf{r}) \simeq \lim_{N\to\infty} \sum_{n=1}^{N} [a_n(\cos\psi_n \cos\phi_n - \sin\psi_n \sin\phi_n \cos\theta_n) \cos(k_i \hat{\mathbf{e}}_n \cdot \mathbf{r} + \beta_n)] \tag{14}$$

$$\Psi_i^{\text{e},z}(\mathbf{r}) \simeq \lim_{N\to\infty} \sum_{n=1}^{N} [a_n \sin\psi_n \sin\theta_n \cos(k_i \hat{\mathbf{e}}_n \cdot \mathbf{r} + \beta_n)]. \tag{15}$$

The polarization angle ψ_n, direction $\hat{\mathbf{e}}_n$ and phase β_n are independent, uniform random variables. The amplitude a_n satisfies $\langle a_m a_n \rangle = \frac{2}{(NV)}\delta_{mn}$, in which V is the volume of the cavity.

Correspondingly, the vector components of magnetic eigenvector Ψ_i^{m} can be approximated as

$$\Psi_i^{\text{m},x}(\mathbf{r}) \simeq \lim_{N\to\infty} \sum_{n=1}^{N} [a_n(\cos\psi_n \cos\phi_n \cos\theta_n - \sin\psi_n \sin\phi_n) \sin(k_i \hat{\mathbf{e}}_n \cdot \mathbf{r} + \beta_n)] \tag{16}$$

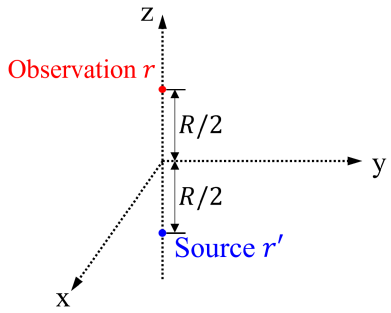

Fig. 2. Notation for the covariance derivation.

$$\Psi_i^{\mathrm{m},y}(\mathbf{r}) \simeq \lim_{N\to\infty}\sum_{n=1}^{N}[a_n(\cos\psi_n\sin\phi_n\cos\theta_n + \sin\psi_n\cos\phi_n)\sin(k_i\hat{\mathbf{e}}_n\cdot\mathbf{r}+\beta_n)] \tag{17}$$

$$\Psi_i^{\mathrm{m},z}(\mathbf{r}) \simeq \lim_{N\to\infty}\sum_{n=1}^{N}[-a_n\cos\psi_n\sin\theta_n\sin(k_i\hat{\mathbf{e}}_n\cdot\mathbf{r}+\beta_n)]. \tag{18}$$

By leveraging the central limit theorem, we note that all three vector components $\Psi_i^{\mathrm{m},x}$, $\Psi_i^{\mathrm{m},y}$, and $\Psi_i^{\mathrm{m},z}$ are zero mean Gaussian random variables. The statistics of the $\mathbf{\Psi}_i^{\mathrm{m}}(\mathbf{r},k_i)\otimes\mathbf{\Psi}_i^{\mathrm{m}}(\mathbf{r}',k_i)$ can be elucidated through the outer product of correlated Gaussian random variables, denoted as $\overline{\mathbf{D}}_{\mathrm{S}}^{\mathrm{mm}}(\mathbf{r},\mathbf{r}';k_i)$. This is achieved using the discrete Karhunen–Loeve expansion, a method well-documented in the literature [35], [36]. Specifically, considering the source point $\mathbf{r}'$ and the observation point $\mathbf{r}$ are located along z-axis, as illustrated in Fig. 2, the covariance function between vectorial components can be derived and the proofs for these derivations are provided in Appendix A

$$\mathcal{C}_{xx}^{\mathrm{mm}}(R) = \langle\Psi_i^{\mathrm{m},x}(\mathbf{r}),\Psi_i^{\mathrm{m},x}(\mathbf{r}')\rangle = \frac{1}{3V}f_{\perp}(k_iR) \tag{19}$$

$$\mathcal{C}_{yy}^{\mathrm{mm}}(R) = \langle\Psi_i^{\mathrm{m},y}(\mathbf{r}),\Psi_i^{\mathrm{m},y}(\mathbf{r}')\rangle = \frac{1}{3V}f_{\perp}(k_iR) \tag{20}$$

$$\mathcal{C}_{zz}^{\mathrm{mm}}(R) = \langle\Psi_i^{\mathrm{m},z}(\mathbf{r}),\Psi_i^{\mathrm{m},z}(\mathbf{r}')\rangle = \frac{1}{3V}f_{//}(k_iR) \tag{21}$$

where the distance $R=|\mathbf{r}-\mathbf{r}'|$, and $f_{\perp}(k_iR)$ and $f_{//}(k_iR)$ represent transversal and longitudinal correlation described by

$$f_{\perp}(k_iR) = \frac{3}{2}\left[\frac{\sin k_iR}{k_iR} - \frac{\sin k_iR - k_iR\cos k_iR}{(k_iR)^3}\right] \tag{22}$$

$$f_{//}(k_iR) = 3\frac{\sin(k_iR)-k_iR\cos(k_iR)}{(k_iR)^3}. \tag{23}$$

The results are essentially the same as the case of electric eigenvectors in [29]. The mean value of the dyadic expression in the numerator of (11) is

$$\begin{aligned}\left\langle\overline{\mathbf{D}}_{\mathrm{S}}^{\mathrm{mm}}(\mathbf{r},\mathbf{r}';k_i)\right\rangle &= \langle\mathbf{\Psi}_i^{\mathrm{m}}(\mathbf{r},k_i)\otimes\mathbf{\Psi}_i^{\mathrm{m}}(\mathbf{r}',k_i)\rangle\\ &= \mathcal{C}_{xx}^{\mathrm{mm}}(R)\hat{\mathbf{x}}\hat{\mathbf{x}}+\mathcal{C}_{yy}^{\mathrm{mm}}(R)\hat{\mathbf{y}}\hat{\mathbf{y}}+\mathcal{C}_{zz}^{\mathrm{mm}}(R)\hat{\mathbf{z}}\hat{\mathbf{z}}\\ &= -\frac{2\pi}{k_iV}\mathrm{Im}\left[\overline{\mathbf{G}}_0^{\mathrm{mm}}(\mathbf{r},\mathbf{r}';k_i)\right]\end{aligned} \tag{24}$$

where $\overline{\mathbf{G}}_0^{\mathrm{mm}}(\mathbf{r},\mathbf{r}')$ is the magnetic dyadic Green's function in free space, defined by

$$\overline{\mathbf{G}}_0^{\mathrm{mm}}(\mathbf{r},\mathbf{r}';k) = \left(\bar{\bar{\mathbf{I}}}+\frac{\nabla\nabla}{k^2}\right)\frac{e^{-jkR}}{4\pi R}. \tag{25}$$

By following the derivation in Section II.B [29], we can derive the magnetic S-DGF as

$$\overline{\mathbf{G}}_{\mathrm{S}}^{\mathrm{mm}}(\mathbf{r},\mathbf{r}') = \mathrm{Re}\left[\overline{\mathbf{G}}_0^{\mathrm{mm}}(\mathbf{r},\mathbf{r}')\right]+\sum_m\frac{\overline{\mathbf{D}}_{\mathrm{S}}^{\mathrm{mm}}(\mathbf{r},\mathbf{r}';k_m)}{\tilde{\lambda}_m-j\alpha}\frac{kV}{2\pi^2}. \tag{26}$$

Next, we will derive Green's dyadic, denoted as $\overline{\mathbf{G}}_{\mathrm{S}}^{\mathrm{me}}$, representing the contribution from the electric current source to the magnetic field. It satisfies

$$\begin{aligned}\overline{\mathbf{G}}_{\mathrm{S}}^{\mathrm{me}}(\mathbf{r},\mathbf{r}') &= \nabla\times\overline{\mathbf{G}}_{\mathrm{S}}^{\mathrm{ee}}(\mathbf{r},\mathbf{r}')\\ &= \sum_i\frac{\nabla\times\mathbf{\Psi}_i^{\mathrm{e}}(\mathbf{r},k_i)\otimes\mathbf{\Psi}_i^{\mathrm{e}}(\mathbf{r}',k_i)}{k^2-k_i^2-j\frac{k^2}{Q_{\mathrm{uni}}}}\\ &= \sum_i\frac{k_i\mathbf{\Psi}_i^{\mathrm{m}}(\mathbf{r},k_i)\otimes\mathbf{\Psi}_i^{\mathrm{e}}(\mathbf{r}',k_i)}{k^2-k_i^2-j\frac{k^2}{Q_{\mathrm{uni}}}}.\end{aligned} \tag{27}$$

To reveal the statistical property of $\overline{\mathbf{G}}_{\mathrm{S}}^{\mathrm{me}}$, we first derive the covariance function between vectorial components of $\mathbf{\Psi}_i^{\mathrm{m}}$ and $\mathbf{\Psi}_i^{\mathrm{e}}$. As is shown in Appendix B, the results are obtained as

$$\mathcal{C}_{xy}^{\mathrm{me}}(R) = \langle\Psi_i^{\mathrm{m},x}(\mathbf{r}),\Psi_i^{\mathrm{e},y}(\mathbf{r}')\rangle = \frac{k_iR}{6V}f_{//}(k_iR) \tag{28}$$

$$\mathcal{C}_{yx}^{\mathrm{me}}(R) = \langle\Psi_i^{\mathrm{m},y}(\mathbf{r}),\Psi_i^{\mathrm{e},x}(\mathbf{r}')\rangle = -\frac{k_iR}{6V}f_{//}(k_iR) \tag{29}$$

$$\mathcal{C}_{xx}^{\mathrm{me}}(R) = \mathcal{C}_{yy}^{\mathrm{me}}(R) = \mathcal{C}_{zz}^{\mathrm{me}}(R) = 0 \tag{30}$$

$$\mathcal{C}_{xz}^{\mathrm{me}}(R) = \mathcal{C}_{zx}^{\mathrm{me}}(R) = \mathcal{C}_{yz}^{\mathrm{me}}(R) = \mathcal{C}_{zy}^{\mathrm{me}}(R) = 0. \tag{31}$$

We recall the expression of the free-space dyadic Green's function $\overline{\mathbf{G}}_0^{\mathrm{me}}(\mathbf{r},\mathbf{r}')$, given by

$$\overline{\mathbf{G}}_0^{\mathrm{me}}(\mathbf{r},\mathbf{r}';k) = \nabla\times\overline{\mathbf{G}}_0^{\mathrm{ee}}(\mathbf{r},\mathbf{r}';k) = \nabla\frac{e^{-jkR}}{4\pi R}\times\bar{\bar{\mathbf{I}}}. \tag{32}$$

The explicit dyadic form of (32) can be written as

$$\overline{\mathbf{G}}_0^{\mathrm{me}}(\mathbf{r},\mathbf{r}';k) = \left(-jk-\frac{1}{R}\right)\frac{e^{-jkR}}{4\pi R}\hat{\mathbf{R}}\times\bar{\bar{\mathbf{I}}}. \tag{33}$$

Regarding the two points given in Fig. 2, we have the real and imaginary parts

$$\mathrm{Re}\left[\overline{\mathbf{G}}_0^{\mathrm{me}}(\mathbf{r},\mathbf{r}';k)\right] = -\frac{kR\sin kR+\cos kR}{4\pi R^2}(\hat{\mathbf{y}}\hat{\mathbf{x}}-\hat{\mathbf{x}}\hat{\mathbf{y}}) \tag{34}$$

$$\mathrm{Im}\left[\overline{\mathbf{G}}_0^{\mathrm{me}}(\mathbf{r},\mathbf{r}';k)\right] = \frac{\sin kR-kR\cos kR}{4\pi R^2}(\hat{\mathbf{y}}\hat{\mathbf{x}}-\hat{\mathbf{x}}\hat{\mathbf{y}}). \tag{35}$$

By comparing (28)–(31) with (35), we have the mean value of the dyadic expression in (27)

$$\begin{aligned}\left\langle\overline{\mathbf{D}}_{\mathrm{S}}^{\mathrm{me}}(\mathbf{r},\mathbf{r}';k_i)\right\rangle &= \langle\mathbf{\Psi}_i^{\mathrm{m}}(\mathbf{r},k_i)\otimes\mathbf{\Psi}_i^{\mathrm{e}}(\mathbf{r}',k_i)\rangle\\ &= \mathcal{C}_{xy}^{\mathrm{me}}(R)\hat{\mathbf{x}}\hat{\mathbf{y}}+\mathcal{C}_{yx}^{\mathrm{me}}(R)\hat{\mathbf{y}}\hat{\mathbf{x}}\\ &= -\frac{2\pi}{k_i^2V}\mathrm{Im}\left[\overline{\mathbf{G}}_0^{\mathrm{me}}(\mathbf{r},\mathbf{r}';k_i)\right].\end{aligned} \tag{36}$$

The mean of stochastic Green's dyadic $\overline{\mathbf{G}}_{\mathrm{S}}^{\mathrm{me}}(\mathbf{r},\mathbf{r}')$ can be obtained as follows:

$$\begin{aligned}\left\langle \overline{\mathbf{G}}_{\mathrm{S}}^{\mathrm{me}}(\mathbf{r},\mathbf{r}')\right\rangle &= \sum_i \frac{k_i \left\langle \overline{\mathbf{D}}_{\mathrm{S}}^{\mathrm{me}}(\mathbf{r},\mathbf{r}';k_i)\right\rangle}{k^2-k_i^2-j\frac{k^2}{Q_{\mathrm{uni}}}} \\ &= -\frac{1}{\pi}\sum_i \Delta(k_i^2)\frac{\mathrm{Im}\left[\overline{\mathbf{G}}_0^{\mathrm{me}}(\mathbf{r},\mathbf{r}';k_i)\right]}{k^2-k_i^2-j\frac{k^2}{Q_{\mathrm{uni}}}} \\ &= \overline{\mathbf{G}}_0^{\mathrm{me}}(\mathbf{r},\mathbf{r}')\,. \end{aligned} \tag{37}$$

In the abovementioned derivation, we have utilized the expression of mean space between two adjacent squared eigenvalues $\Delta(k_i^2)=2\pi^2/(k_iV)$, the Sokhotski–Plemelj theorem for the real line, and the Kramer–Kronig relation between the real part and imaginary part of $\overline{\mathbf{G}}_0^{\mathrm{me}}(\mathbf{r},\mathbf{r}')$. Finally, the Green's dyadic $\overline{\mathbf{G}}_{\mathrm{S}}^{\mathrm{me}}(\mathbf{r},\mathbf{r}')$ can be constructed as

$$\overline{\mathbf{G}}_{\mathrm{S}}^{\mathrm{me}}(\mathbf{r},\mathbf{r}')=\mathrm{Re}\left[\overline{\mathbf{G}}_0^{\mathrm{me}}(\mathbf{r},\mathbf{r}')\right]+\sum_m \frac{\overline{\mathbf{D}}_{\mathrm{S}}^{\mathrm{me}}(\mathbf{r},\mathbf{r}';k_m)}{\tilde{\lambda}_m-j\alpha}\frac{k^2\,V}{2\pi^2}. \tag{38}$$

The Green's dyadic $\overline{\mathbf{G}}_{\mathrm{S}}^{\mathrm{em}}(\mathbf{r},\mathbf{r}')$ has the same expression as $\overline{\mathbf{G}}_{\mathrm{S}}^{\mathrm{me}}(\mathbf{r},\mathbf{r}')$ based on the duality principle.

D. Analysis of Electric Dipoles Inside Enclosures

The electric S-DGF can be directly utilized to analyze electric dipole problems shown in Fig. 1. Specifically, we consider the Tx dipole characterized by a thin, short conducting wire of length l placed inside a 3-D metallic enclosure. In this scenario, both the electrical length and the radius of the wire are significantly smaller than the wavelength, allowing us to apply the thin-wire approximation. We assume that the electric current on the dipole follows a vector triangle function, denoted as $\mathbf{v}^{\mathrm{t}}(\mathbf{r}')$, with the peak current at the center represented by $\mathrm{J_t}$. The radiated E-field can be expressed using the electric field integral equation (EFIE)

$$\mathbf{E}_{\mathrm{S}}(\mathbf{r}) = j\omega\mu\int \overline{\mathbf{G}}_{\mathrm{S}}^{\mathrm{ee}}(\mathbf{r},\mathbf{r}')\cdot\left[\mathbf{v}^{\mathrm{t}}(\mathbf{r}')\,\mathrm{J_t}\right]d\mathbf{r}'. \tag{39}$$

The Tx dipole acts as the source to generate the stochastic EM field within the cavity. We may introduce another small electric dipole as an Rx probe device. Utilizing the Galerkin method and vector triangle basis and testing functions, the EFIE can be formulated as $[\mathrm{Z_S}]\cdot\mathrm{J_r}=[\mathrm{C_S}]\cdot\mathrm{J_t}$, where $\mathrm{J_r}$ is the electric current at the center of the Rx dipole. The self-term and coupling-term impedances are determined by the following expressions:

$$\mathrm{Z_S} = j\omega\mu\int \mathbf{v}^{\mathrm{r}}(\mathbf{r})\cdot\int \overline{\mathbf{G}}_{\mathrm{S}}^{\mathrm{ee}}(\mathbf{r},\mathbf{r}')\cdot\mathbf{v}^{\mathrm{r}}(\mathbf{r}')d\mathbf{r}'d\mathbf{r} \tag{40}$$

$$\mathrm{C_S} = -j\omega\mu\int \mathbf{v}^{\mathrm{r}}(\mathbf{r})\cdot\int \overline{\mathbf{G}}_{\mathrm{S}}^{\mathrm{ee}}(\mathbf{r},\mathbf{r}')\cdot\mathbf{v}^{\mathrm{t}}(\mathbf{r}')d\mathbf{r}'d\mathbf{r}. \tag{41}$$

Substituting (7) into (40) and (41), we can obtain the explicit form of $\mathrm{Z_S}$ and $\mathrm{C_S}$ as (see Appendix C for detailed derivation)

$$\mathrm{Z_S} = j\mathrm{X}_0^{\mathrm{r}} + \frac{j}{\pi}\sum_m \sqrt{\mathrm{R}_0^{\mathrm{r}}}\cdot\frac{(w_m^{\mathrm{r}})^2}{\tilde{\lambda}_m-j\alpha}\cdot\sqrt{\mathrm{R}_0^{\mathrm{r}}}$$

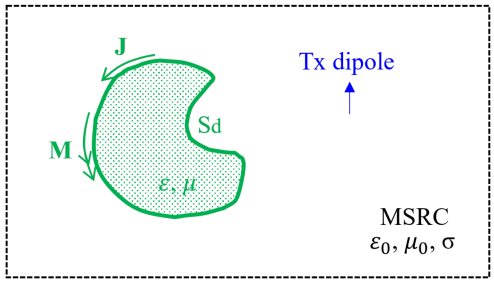

Fig. 3. Notations for the cavity dielectric loading problem.

$$\mathrm{C_S} = -\frac{j}{\pi}\sum_m \sqrt{\mathrm{R}_0^{\mathrm{r}}}\cdot\frac{w_m^{\mathrm{r}}w_m^{\mathrm{t}}}{\tilde{\lambda}_m-j\alpha}\cdot\sqrt{\mathrm{R}_0^{\mathrm{t}}}$$

where $\mathrm{R}_0^{\mathrm{r}}$ and $\mathrm{X}_0^{\mathrm{r}}$ are the real and imaginary parts of the dipole impedance, $\mathrm{Z}_0^{\mathrm{r}}=j\mathrm{X}_0^{\mathrm{r}}+\mathrm{R}_0^{\mathrm{r}}$, using free-space dyadic Green's function as the kernel. w_m^{r} and w_m^{t} represent independent, zero mean, unit variance Gaussian random variables.

In order to measure received vectorial E-fields, we can place three independent Rx dipoles along with the $\hat{\mathbf{x}}$-, $\hat{\mathbf{y}}$-, and $\hat{\mathbf{z}}$-axis, respectively. The resulting matrix equation is given by

$$\begin{bmatrix}\mathrm{Z_S^{x,x}} & & \\ & \mathrm{Z_S^{y,y}} & \\ & & \mathrm{Z_S^{z,z}}\end{bmatrix}\cdot\begin{bmatrix}\mathrm{J_r^x}\\ \mathrm{J_r^y}\\ \mathrm{J_r^z}\end{bmatrix} = \begin{bmatrix}\mathrm{C_S^{x,t}}\\ \mathrm{C_S^{y,t}}\\ \mathrm{C_S^{z,t}}\end{bmatrix}\cdot\mathrm{J_t}. \tag{42}$$

Equation (42) can be straightforwardly extended to include many Rx dipoles inside the enclosure.

E. Analysis of Cavity Dielectric Loading

Considering a homogeneous dielectric object illuminated by an electric dipole inside the enclosure, as shown in Fig. 3. The boundary of the dielectric object is denoted as S_{d}. The boundary value problem can be decomposed into the interior subproblem, i.e., the solution of the wave equation within the dielectric object, and the exterior subproblem with the wave solution exterior to the dielectric object. The entire domain solution is obtained by the enforcement of electric and magnetic field continuities across the bounding surface of the dielectric object.

In this work, we employ a surface IE method known as the Poggio–Miller–Chang–Harrington–Wu–Tsai (PMCHWT) formulation [37] to analyze the dielectric object. The homogeneous (DGF) is utilized for the interior dielectric subregion, while the stochastic DGF is employed for the cavity subregion outside of the dielectric object.

Regarding the interior dielectric subregion, we have EFIE and magnetic field integral equation (MFIE) using Green's function in the homogeneous dielectric medium

$$\begin{aligned}\mathbf{E}(\mathbf{r}) &= j\omega\mu\iint \overline{\mathbf{G}}_{\mathrm{H}}^{\mathrm{ee}}(\mathbf{r},\mathbf{r}')\cdot\mathbf{J}(\mathbf{r}')\,d\mathbf{S}' \\ &\quad+\iint \overline{\mathbf{G}}_{\mathrm{H}}^{\mathrm{em}}(\mathbf{r},\mathbf{r}')\cdot\mathbf{M}(\mathbf{r}')\,d\mathbf{S}' \\ \mathbf{H}(\mathbf{r}) &= \iint \overline{\mathbf{G}}_{\mathrm{H}}^{\mathrm{me}}(\mathbf{r},\mathbf{r}')\cdot\mathbf{J}(\mathbf{r}')\,d\mathbf{S}'\end{aligned} \tag{43}$$

$$+ j\omega\epsilon \iint \overline{\mathbf{G}}_{\mathrm{H}}^{\mathrm{mm}}(\mathbf{r},\mathbf{r}') \cdot \mathbf{M}(\mathbf{r}')\, d\mathbf{S}'. \tag{44}$$

For the cavity subregion, we have EFIE and MFIE using the SGF

$$\begin{aligned}\mathbf{E}_{\mathrm{S}}(\mathbf{r}) &= j\omega\mu_0 \iint \overline{\mathbf{G}}_{\mathrm{S}}^{\mathrm{ee}}(\mathbf{r},\mathbf{r}') \cdot \mathbf{J}(\mathbf{r}')\, d\mathbf{S}' \\ &\quad + \iint \overline{\mathbf{G}}_{\mathrm{S}}^{\mathrm{em}}(\mathbf{r},\mathbf{r}') \cdot \mathbf{M}(\mathbf{r}')\, d\mathbf{S}' \qquad (45)\\ \mathbf{H}_{\mathrm{S}}(\mathbf{r}) &= \iint \overline{\mathbf{G}}_{\mathrm{S}}^{\mathrm{me}}(\mathbf{r},\mathbf{r}') \cdot \mathbf{J}(\mathbf{r}')\, d\mathbf{S}' \\ &\quad + j\omega\epsilon_0 \iint \overline{\mathbf{G}}_{\mathrm{S}}^{\mathrm{mm}}(\mathbf{r},\mathbf{r}') \cdot \mathbf{M}(\mathbf{r}')\, d\mathbf{S}'. \qquad (46)\end{aligned}$$

To derive the discrete matrix equation, the dielectric surface S_{d} is discretized using a collection of triangular meshes denoted by $\mathcal{K}^h$. Both trial and test functions employ the surface div-conforming vector Rao–Wilton–Glisson (RWG) functions [38], $\mathbf{v}^h$, which are defined over $\mathcal{K}^h$.

By applying the interface conditions, i.e., tangential continuities of EM fields across the dielectric boundary, and Galerkin testing method [39], the surface IE in (43), (44), (45), and (46) can be represented in a matrix equation as

$$\begin{bmatrix} \mathbf{Z}_{\mathrm{S}}^{\mathrm{e,j}} + \mathbf{Z}_{\mathrm{H}}^{\mathrm{e,j}} & \mathbf{Z}_{\mathrm{S}}^{\mathrm{e,m}} + \mathbf{Z}_{\mathrm{H}}^{\mathrm{e,m}} \\ \mathbf{Z}_{\mathrm{S}}^{\mathrm{h,j}} + \mathbf{Z}_{\mathrm{H}}^{\mathrm{h,j}} & \mathbf{Z}_{\mathrm{S}}^{\mathrm{h,m}} + \mathbf{Z}_{\mathrm{H}}^{\mathrm{h,m}} \end{bmatrix} \begin{bmatrix} \mathbf{J}_{\mathrm{d}} \\ \mathbf{M}_{\mathrm{d}} \end{bmatrix} = \begin{bmatrix} \mathbf{C}_{\mathrm{S}}^{\mathrm{e,t}} \cdot \mathrm{J}_{\mathrm{t}} \\ \mathbf{C}_{\mathrm{S}}^{\mathrm{h,t}} \cdot \mathrm{J}_{\mathrm{t}} \end{bmatrix}. \tag{47}$$

The impedance submatrix blocks labeled with subscript S utilize the SGF as the integral kernel, while those marked with H utilize the homogeneous Green's function of the dielectric medium. The $\mathbf{J}_{\mathrm{d}}$ and $\mathbf{M}_{\mathrm{d}}$ represent the solution vectors for surface electric and magnetic currents on the dielectric surface S_{d}. The right-hand side characterizes the cavity electric and magnetic fields radiated from the electric dipole. The explicit expression of (47) is provided in Appendix D.

F. Calculation of Statistical Cavity Q-factor

We are now ready to analyze the statistical cavity Q-factor for the problem statement illustrated in Fig. 1. The wave physics involving the Tx dipole, Rx dipoles, and the dielectric object is modeled by an IE matrix equation of the following compact form:

$$\begin{bmatrix} \mathbf{Z}_{\mathrm{S}}^{\mathrm{e,j}}+\mathbf{Z}_{\mathrm{H}}^{\mathrm{e,j}} & \mathbf{Z}_{\mathrm{S}}^{\mathrm{e,m}}+\mathbf{Z}_{\mathrm{H}}^{\mathrm{e,m}} & \mathbf{C}_{\mathrm{S}}^{\mathrm{e,x}} & \mathbf{C}_{\mathrm{S}}^{\mathrm{e,y}} & \mathbf{C}_{\mathrm{S}}^{\mathrm{e,z}} \\ \mathbf{Z}_{\mathrm{S}}^{\mathrm{h,j}}+\mathbf{Z}_{\mathrm{H}}^{\mathrm{h,j}} & \mathbf{Z}_{\mathrm{S}}^{\mathrm{h,m}}+\mathbf{Z}_{\mathrm{H}}^{\mathrm{h,m}} & \mathbf{C}_{\mathrm{S}}^{\mathrm{h,x}} & \mathbf{C}_{\mathrm{S}}^{\mathrm{h,y}} & \mathbf{C}_{\mathrm{S}}^{\mathrm{h,z}} \\ \mathbf{C}_{\mathrm{S}}^{\mathrm{x,j}} & \mathbf{C}_{\mathrm{S}}^{\mathrm{x,m}} & \mathbf{Z}_{\mathrm{S}}^{\mathrm{x,x}} & & \\ \mathbf{C}_{\mathrm{S}}^{\mathrm{y,j}} & \mathbf{C}_{\mathrm{S}}^{\mathrm{y,m}} & & \mathbf{Z}_{\mathrm{S}}^{\mathrm{y,y}} & \\ \mathbf{C}_{\mathrm{S}}^{\mathrm{z,j}} & \mathbf{C}_{\mathrm{S}}^{\mathrm{z,m}} & & & \mathbf{Z}_{\mathrm{S}}^{\mathrm{z,z}} \end{bmatrix} \begin{bmatrix} \mathbf{J}_{\mathrm{d}} \\ \mathbf{M}_{\mathrm{d}} \\ \mathbf{J}_{\mathrm{r}}^{\mathrm{x}} \\ \mathbf{J}_{\mathrm{r}}^{\mathrm{y}} \\ \mathbf{J}_{\mathrm{r}}^{\mathrm{z}} \end{bmatrix}$$

$$= \begin{bmatrix} \mathbf{C}_{\mathrm{S}}^{\mathrm{e,t}} \cdot \mathrm{J}_{\mathrm{t}} & \mathbf{C}_{\mathrm{S}}^{\mathrm{h,t}} \cdot \mathrm{J}_{\mathrm{t}} & \mathbf{C}_{\mathrm{S}}^{\mathrm{x,t}} \cdot \mathrm{J}_{\mathrm{t}} & \mathbf{C}_{\mathrm{S}}^{\mathrm{y,t}} \cdot \mathrm{J}_{\mathrm{t}} & \mathbf{C}_{\mathrm{S}}^{\mathrm{z,t}} \cdot \mathrm{J}_{\mathrm{t}} \end{bmatrix}^T. \tag{48}$$

In (48), $\mathbf{J}_{\mathrm{r}}^{\mathrm{x/y/z}}$ are the solution vectors of electric current for a finite number N sets of $\hat{\mathbf{x}}$-, $\hat{\mathbf{y}}$-, and $\hat{\mathbf{z}}$- directed Rx dipoles. In addition to the matrix blocks described in previous sections, we have introduced matrices $\mathbf{C}_{\mathrm{S}}^{\mathrm{e/h,x/y/z}}$ accounting for the coupling between the dielectric surface currents and Rx dipole sets. It is noted that there are no coupling terms between Rx dipoles, as they are used as probing devices.

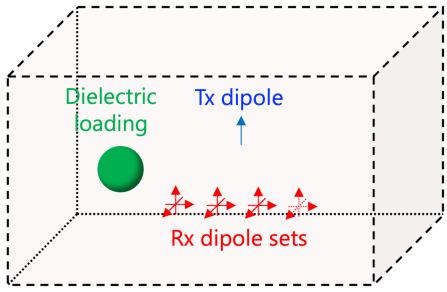

Fig. 4. Illustration of the reduced-order model for the dielectric loading problem.

We remark that the matrix equation (48) only involves the wire currents on the Tx/Rx dipoles and the surface currents on the dielectric surface. The coupling between these currents and their interaction with the cavity interior are statistically characterized through the S-DGF model. Therefore, this is no need for the discretization of the cavity enclosure and mode stirrer. Compared to the original problem statement in Fig. 1, the reduced-order model is illustrated in Fig. 4.

After obtaining the solution of (48), the dissipated power $P_{d,\mathrm{abl}}$ is then calculated by integrating the Poynting vector over the surface of the dielectric object, that is

$$P_{d,\mathrm{abl}} = \frac{1}{2}\mathrm{Re}\left[\sum_i \iint \mathbf{J}_i^d \times \mathbf{n}_i \cdot \left(\mathbf{M}_i^d\right)^* d\mathrm{S}_i\right] \tag{49}$$

where $\mathbf{M}_i^d$ and $\mathbf{J}_i^d$ represent the surface electric and magnetic currents on each triangle. $\mathbf{n}_i$ is the corresponding normal direction.

Given the use of linear triangular basis functions for the Rx dipole currents, retrieving the vectorial E-field from the electric current solution is straightforward. For example, the $\hat{\mathbf{x}}$-directed E-fields at Rx probe locations can be obtained by

$$\mathbf{E}^{\mathrm{x}} = \frac{2}{l}\mathbf{Z}_S^{\mathrm{x,x}} \cdot \mathbf{J}_{\mathrm{r}}^{\mathrm{x}}. \tag{50}$$

Subsequently, the cavity energy density can be approximated by

$$W_c = \frac{\epsilon}{N}\left[(\mathbf{E}^{\mathrm{x}})^T \cdot (\mathbf{E}^{\mathrm{x}})^* + (\mathbf{E}^{\mathrm{y}})^T \cdot (\mathbf{E}^{\mathrm{y}})^* + (\mathbf{E}^{\mathrm{z}})^T \cdot (\mathbf{E}^{\mathrm{z}})^*\right]. \tag{51}$$

The energy stored in the cavity is calculated as $U_s = W_c \cdot V$. Finally, the cavity Q-factor due to the absorptive dielectric loading is obtained by using (2)

$$Q_{\mathrm{abl}}(\omega) = \omega\frac{U_s}{P_{d,\mathrm{abl}}}. \tag{52}$$

By repeating the abovementioned procedure with different S-DGF IE matrices, we can predict the statistics of cavity Q-factor due to the dielectric loading.

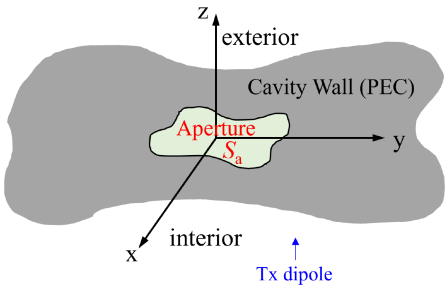

Fig. 5. Illustration of the aperture leakage problem.

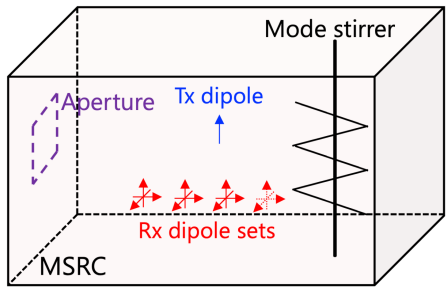

Fig. 6. Illustration of the design of the numerical experiment for the aperture leakage problem.

III. Extension to Other Localized Losses

A. Extension to Aperture Leakage

1) Surface IE Formulation for Aperture: Consider a locally quasi-planar cavity wall with an irregular aperture situated in the xy-plane, as illustrated in Fig. 5. The surface of the aperture opening is represented by S_a. The objective is to calculate the surface magnetic current $\mathbf{M} = \mathbf{E} \times \hat{\mathbf{z}}$ at the aperture, induced by an internal Tx dipole inside the cavity.

Based on the equivalence principle, an equivalent interior problem can be derived by considering the aperture covered by a PEC [40]. At the aperture surface, the magnetic field relation is expressed as

$$\mathbf{H}_t^- (\mathbf{r}) = 2\mathbf{H}_t^{\mathrm{Tx}} (\mathbf{r}) + \mathbf{H}_t^{\mathrm{R},-} (\mathbf{r}) \ \text{ on } S_a. \tag{53}$$

Here, $\mathbf{H}_t^-$ represents the tangential components of the total magnetic field. The $\mathbf{H}_t^{\mathrm{Tx}}$ denotes the tangential components of the magnetic field radiated by the Tx dipole. The $\mathbf{H}_t^{\mathrm{R},-}$ represents the tangential components of the radiated magnetic field by the surface magnetic current $\mathbf{M}$

$$\mathbf{H}_t^{\mathrm{R},-}(\mathbf{r}) = -2\frac{jk_0}{\eta}\pi_\tau \left(\iint_{S_a} \overline{\mathbf{G}}_{\mathrm{S}}^{\mathrm{mm}}(\mathbf{r},\mathbf{r}') \cdot \mathbf{M}(\mathbf{r}')\, dS' \right) \tag{54}$$

where the $\eta = \sqrt{\frac{\mu}{\epsilon}}$ is the wave impedance, $\pi_\tau(\bullet)$ is a tangential trace operator defined by: $\pi_\tau(\mathbf{u}) := \hat{\mathbf{n}} \times (\mathbf{u} \times \hat{\mathbf{n}})|_{S_a}$.

Another equivalent problem can be established for the exterior region by filling the interior cavity region with a PEC. The aperture surface IE for the exterior region in terms of the magnetic field is given by

$$\mathbf{H}_t^{\mathrm{R},+} (\mathbf{r}) = 2\frac{jk_0}{\eta}\pi_\tau \left(\iint_{S_a} \overline{\mathbf{G}}_0^{\mathrm{mm}}(\mathbf{r},\mathbf{r}') \cdot \mathbf{M}(\mathbf{r}')\, dS' \right). \tag{55}$$

Finally, by applying the boundary condition at the aperture, i.e., the continuity of magnetic fields for exterior and interior regions, $\mathbf{H}_t^+(\mathbf{r}) (:= \mathbf{H}_t^{\mathrm{R},+}) = \mathbf{H}_t^-(\mathbf{r})$, we have

$$\mathbf{H}^{\mathrm{R},+} (\mathbf{r}) - \mathbf{H}^{\mathrm{R},-}(\mathbf{r}) = 2\mathbf{H}_t^{\mathrm{Tx}} (\mathbf{r}) \ \text{ on } S_a. \tag{56}$$

To derive the discrete matrix equation, the aperture surface S_a is discretized using triangular elements denoted by $\mathcal{K}^h$. Both trial and test functions make use of the RWG functions $\mathbf{v}^h$ defined over $\mathcal{K}^h$. Through the application of interface condition and Galerkin testing method [39], the SIEs in (54), (55), and (56) can be expressed in a matrix equation as

$$[\mathbf{Y}_0^{\mathrm{a}} + \mathbf{Y}_{\mathrm{S}}^{\mathrm{a}}] \cdot \mathbf{M}_a = \mathbf{C}_{\mathrm{S}}^{\mathrm{a,t}} \cdot \mathrm{J_t}. \tag{57}$$

Here, $\mathbf{M}_a$ is the solution vector for the magnetic current at the aperture. $\mathbf{Y}_0^{\mathrm{a}}$ is the aperture admittance matrix for the exterior region in terms of free-space dyadic Green's function, which is calculated by

$$\mathbf{Y}_0^{\mathrm{a}} = 2\frac{jk_0}{\eta} \iint_{\mathcal{K}^h} \iint_{\mathcal{K}^h} \mathbf{v}^h(\mathbf{r}) \cdot \left[\overline{\overline{\mathbf{G}}}_0(\mathbf{r},\mathbf{r}') \cdot \mathbf{v}^h(\mathbf{r}') \right] dS' dS. \tag{58}$$

The matrix $\mathbf{Y}_0^{\mathrm{a}}$ consists of real and imaginary parts, expressed as $\mathbf{Y}_0^{\mathrm{a}} = \mathbf{R}_0^{\mathrm{a}} + j\mathbf{X}_0^{\mathrm{a}}$. Following the steps outlined in Appendix F [29], we can construct the aperture admittance matrix $\mathbf{Y}_S^{\mathrm{a}}$ for the interior cavity region

$$\mathbf{Y}_S^{\mathrm{a}} = j\mathbf{X}_0^{\mathrm{a}} + \frac{j}{\pi} \sum_m \sqrt{\mathbf{R}_0^{\mathrm{a}}} \cdot \frac{\boldsymbol{w}_m^{\mathrm{a}} \cdot (\boldsymbol{w}_m^{\mathrm{a}})^T}{\tilde{\lambda}_m - j\alpha} \cdot \sqrt{\mathbf{R}_0^{\mathrm{a}}}. \tag{59}$$

The coupling matrix between the Tx dipole and aperture currents is given as

$$\mathbf{C}_{\mathrm{S}}^{\mathrm{a,t}} = -\frac{j}{\pi} \sum_m \sqrt{\mathbf{R}_0^{\mathrm{a}}} \cdot \frac{\boldsymbol{w}_m^{\mathrm{a}} \cdot (w_m^{\mathrm{t}})}{\tilde{\lambda}_m - j\alpha} \cdot \sqrt{\mathrm{R}_0^{\mathrm{t}}}. \tag{60}$$

The solution of the aperture magnetic current can then be used to analyze the power leakage from the aperture.

2) Calculation of Statistical Cavity Q-factor: To analyze the statistical cavity Q-factor for aperture leakage, the design of the numerical experiment is illustrated in Fig. 6. By leveraging the proposed statistical surrogate model using S-DGF, the wave physics associated with the Tx dipole, Rx dipoles, and the aperture is modeled by an IE matrix equation of the following compact form:

$$\begin{bmatrix} \mathbf{Y}_0^{\mathrm{a}} + \mathbf{Y}_{\mathrm{S}}^{\mathrm{a}} & \mathbf{C}_{\mathrm{S}}^{\mathrm{a,x}} & \mathbf{C}_{\mathrm{S}}^{\mathrm{a,y}} & \mathbf{C}_{\mathrm{S}}^{\mathrm{a,z}} \\ \mathbf{C}_{\mathrm{S}}^{\mathrm{x,a}} & \mathbf{Z}_{\mathrm{S}}^{\mathrm{x,x}} & & \\ \mathbf{C}_{\mathrm{S}}^{\mathrm{y,a}} & & \mathbf{Z}_{\mathrm{S}}^{\mathrm{y,y}} & \\ \mathbf{C}_{\mathrm{S}}^{\mathrm{z,a}} & & & \mathbf{Z}_{\mathrm{S}}^{\mathrm{z,z}} \end{bmatrix} \begin{bmatrix} \mathbf{M}_a \\ \mathbf{J}_{\mathrm{r}}^{\mathrm{x}} \\ \mathbf{J}_{\mathrm{r}}^{\mathrm{y}} \\ \mathbf{J}_{\mathrm{r}}^{\mathrm{z}} \end{bmatrix} = \begin{bmatrix} \mathbf{C}_{\mathrm{S}}^{\mathrm{a,t}} \\ \mathbf{C}_{\mathrm{S}}^{\mathrm{x,t}} \\ \mathbf{C}_{\mathrm{S}}^{\mathrm{y,t}} \\ \mathbf{C}_{\mathrm{S}}^{\mathrm{z,t}} \end{bmatrix} \cdot \mathrm{J_t}. \tag{61}$$

After obtaining the solution of (61), the power leakage through the aperture can be calculated as

$$P_{d,\mathrm{lkg}} = \frac{1}{2}\mathrm{Re}[\mathbf{M}_a^T \cdot (\mathbf{Y}_0^{\mathrm{a}})^* \cdot \mathbf{M}_a^*]. \tag{62}$$

Following the similar procedure given in Section II-F, the probabilistic Q-factor (Q_{lkg}) caused by aperture leakage can be generated.

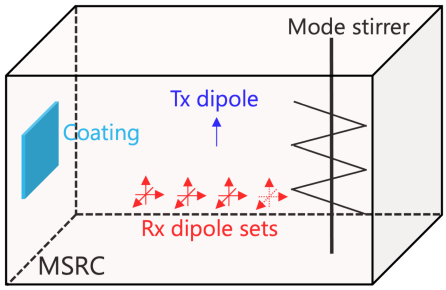

Fig. 7. Illustration of the design of the numerical experiment for Q_{wcl}.

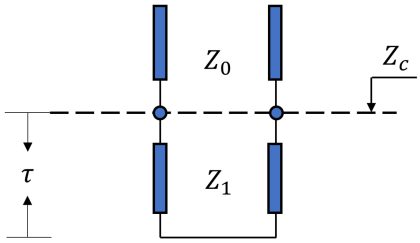

Fig. 8. Transmission line analogy for EM reflection from coated surfaces.

B. Extension to Wall Coating

We extend our methodology to predict the statistical properties of the Q-factor, denoted as Q_{wcl}, attributed to the presence of a localized wall coating. In Fig. 7, we observe the application of a lossy, thin coating on the cavity wall. This coating consists of a single layer of dense dielectric material with a high dielectric constant. The thickness of the coating layer is denoted as τ.

In the subsequent analysis, particularly when dealing with a dielectric material characterized by a high relative permittivity, we utilize the equivalent surface impedance of the coating, denoted as Z_c. To provide a visual representation of this concept, refer to the transmission line analogy depicted in Fig. 8. For the details of the impedance calculation, readers are directed to [41, Table I].

In comparison to the aperture leakage problem elaborated in the previous section, the wall coating problem exhibits a similar reduced-order model and the corresponding surface IE matrix equation. The distinction arises from the admittance matrix governing the relationship between the electric current $\mathbf{J}$ and the magnetic current $\mathbf{M}$ on the coating surface. By using the equivalent impedance Z_c, we have the following impedance boundary condition at the coating surface

$$Z_c\mathbf{J} - \hat{\mathbf{n}} \times \mathbf{M} = 0. \tag{63}$$

Through the Galerkin testing method, the admittance matrix for the coating region can be described as

$$\mathbf{Y}_0^{\text{c}} = \frac{1}{Z_c}\mathbf{G}_m. \tag{64}$$

Here, $\mathbf{G}_m$ is a Gram matrix, with matrix entries determined by the inner product of the testing and basis RWG functions. We can then replace the matrix $\mathbf{Y}_0^{\text{a}}$ by $\mathbf{Y}_0^{\text{c}}$ in (61) to obtain the surface IE matrix equation for the system model.

Following the same procedure described in the previous section, we can generate samples of cavity Q-factor, Q_{wcl}, due to the wall coating.

IV. Further Technical Discussion

A. Impact of the Choice of α

Initially, it may seem counterintuitive that the construction of the S-DGF in (7) also requires an input parameter known as the cavity loss-parameter α. It is crucial to note, however, that the choice of α does not affect the statistical distribution of the calculated cavity Q-factor due to localized losses. This can be explained as follows. The parameter α is related to the Q-factor, Q_{uni}, which is related to the uniform loss of the cavity. In this article, the stochastic Q-factor of the localized losses is directly calculated by $Q_{\text{loc}}(\omega) = \omega U_s / P_{d,\text{loc}}$. As we are solving a coupled stochastic system of equations involving the Tx dipole, Rx dipoles, and lossy components, different α values give rise to different cavity E-field solutions. But both the stored energy (numerator) and dissipated power (denominator) in (2) are proportional to the E-field square. Thereby, the calculated statistical cavity Q-factor due to localized losses remains unaffected by the choice of α.

The methodology can be conceptually compared to the absorbing cross-section (ACS) measurement of dielectric loading in reverberation chambers. For each mode stirrer configuration, the cavity stored energy is expressed as $U = \epsilon \left\langle |\mathbf{E}_c|^2 \right\rangle V$, where $\left\langle |\mathbf{E}_c|^2 \right\rangle$ is the spatial averaged squared magnitude of the cavity E-field, also known as the chamber constant. The dissipated power due to dielectric loss is denoted by $P_d = \sigma_a \left\langle |\mathbf{E}_c|^2 \right\rangle / \eta$, in which σ_a is the ACS of the dielectric loading. As both U and P_d are contingent on the chamber constant, the ACS value calculated by the ratio of dissipated power to stored energy is related to the dielectric object itself, independent of the specific reverberation chambers under consideration.

B. Applicability of the Proposed Work

The research results are particularly relevant in the context of electrically large cavities exhibiting high modal density and modal overlap. In such scenarios, where a macroscopic cavity Q-factor is more relevant than the modal Q-factor, the proposed methodology is shown to be useful and valuable. It is essential to emphasize that, owing to the stochastic nature of the S-DGF, the results do not provide precise Q-factor values for a specific, well-defined cavity geometry or locations of the lossy components. Instead, they provide predictions for the probability distribution of the cavity Q-factor across an ensemble of statistically similar cavity environments.

V. Verification and Validation

A. Verification of Cavity Q-Factor for Absorptive Loading

1) Problem Description: The first numerical study concerns the cavity Q-factor resulting from power dissipation under lossy objects within the enclosure. The goal is to validate the predicted statistics of Q-factor with full-wave numerical simulations.

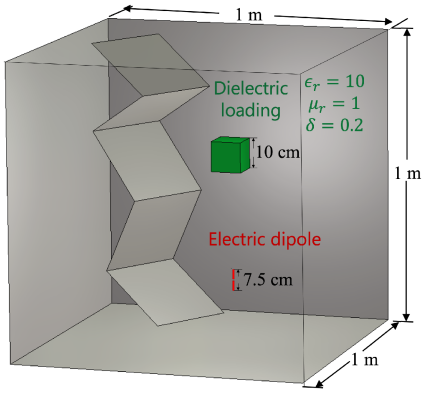

Fig. 9. Illustration of the numerical experiment setup.

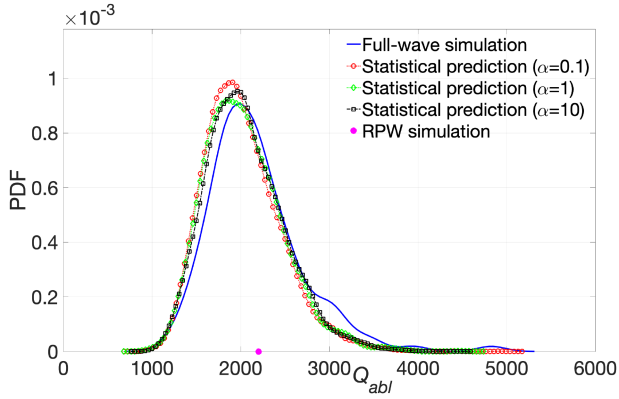

Fig. 10. PDF of the cavity Q-factor for dielectric cube loading.

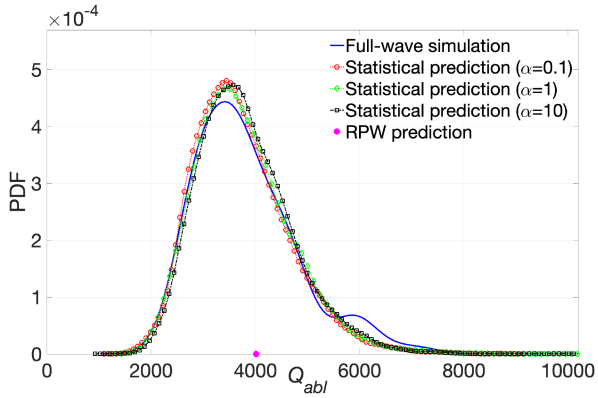

Fig. 11. PDF of the cavity Q-factor for dielectric sphere loading.

The numerical experiment setup is illustrated in Fig. 9. The dimension of the cavity is $1\,\mathrm{m} \times 1\,\mathrm{m} \times 1\,\mathrm{m}$ in length, width, and height. The cavity wall is treated as the PEC boundary condition. An electric dipole of length $l = 7.5\,\mathrm{cm}$ directed along with $\hat{\mathbf{z}}$-axis is used as the cavity excitation. The cavity is loaded with a dielectric cube of size $0.1\,\mathrm{m}$ and constitutive parameters, $\epsilon_r = 10$, $\mu_r = 1$, and loss tangent $\delta = 0.2$. To generate a configuration ensemble, we have included an irregular Z-folded stirrer consisting of five $0.3\,\mathrm{m} \times 0.3\,\mathrm{m}$ metallic plates that are arranged in different folding angles. The center of the stirrer is located at $x = -0.25\,\mathrm{m}$ and $y = -0.25\,\mathrm{m}$.

2) Numerical Approaches: We have considered the following three numerical approaches to characterize the cavity Q-factor. In the first approach, we conduct full-wave simulations using commercial software. The mode stirrer is rotated through 12 positions over 360° for a frequency range of 1.99 to 2.01 GHz with 2 MHz frequency stepping. At each stirrer position and frequency, we uniformly collect E-fields within the cavity to compute the stored energy stored U_s, and the S-parameter S_{11} of the radiating dipole. The dissipated power is then approximated by the radiated power as $P_d \approx P_t = 1 - |S_{11}|^2$. The total number of cavity Q-factor samples is 132, obtained using (1).

As an additional comparison, we explore the well-known random plane wave (RPW) [42] approach, which has been applied to determine the absorption cross section of lossy materials under a random field excitation [43]. The mean-value ACS, $\langle \sigma_a \rangle$, is obtained by averaging $M = 5000$ RPW simulations. Each full-wave simulation uses $N_p = 100$ RPWs as excitation and is solved by the PMCHWT IE matrix equation. Consequently, a deterministic Q-factor, denoted as $\bar{Q}_{\mathrm{abl}}$, is obtained using the formula

$$\bar{Q}_{\mathrm{abl}} = \frac{2\pi V}{\lambda \langle \sigma_a \rangle_M}. \tag{65}$$

The third approach utilizes the proposed work for the statistical prediction of cavity Q-factor for absorptive loading. We employ electrically small electric dipoles of length $l = 5\,\mathrm{mm}$ as both the cavity excitation and E-field probes. These dipoles are modeled by the EFIE (42). The dielectric loading is modeled by the PMCHWT (47), incorporating both the homogeneous DGF and stochastic DGF as integral kernels. The overall system of matrix equation is provided in (48). To verify the assertion that the choice of α in the S-DGF does not affect the PDF of calculated cavity Q-factor, we have considered three different choices, $\alpha = 0.1$, 1, and 10, corresponding to a cavity factor $Q_{\mathrm{uni}} = 37311.11$, 3731.11, 373.11 for homogeneous, uniform loss. A statistical ensemble of S-DGF IE matrices in (48) was generated using 5000 GOE random matrices with dimensions of 2000×2000. This results in a total number of 5000 Q_{abl} samples.

3) Comparison: The PDF of cavity Q-factor obtained from full-wave simulation and the proposed work are plotted in Fig. 10. The mean value of Q_{abl} predicted by the RPW approach is also included. As is seen in Fig. 10, the results show generally good agreement between the first-principles simulation and the statistical prediction. Next, we replace the dielectric cube with a dielectric sphere loading of diameter $0.1\,\mathrm{m}$. The same constitutive parameters are used. The comparison of full-wave simulation, RPW approach, and the proposed work is shown in Fig. 11. The results again agree well.

Table I presents quantitative measures for comparing the mean values and probability distributions obtained through both full-wave simulation and the proposed methodology. The PDF obtained from the full-wave simulation serves as the reference distribution for comparison. Statistical distance is evaluated using the Kullback–Leibler Divergence metric [44]. The results indicate a generally good agreement between the results of the first-principles simulation and the statistical predictions. The

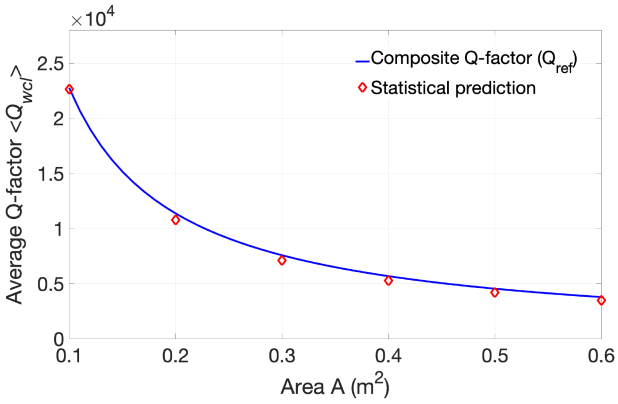

Fig. 12. Comparison of the cavity Q-factor for wall coating case.

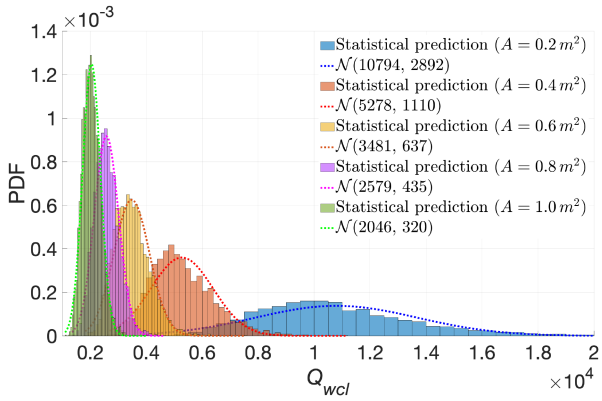

Fig. 13. PDFs of Q-factor as the wall coating area increases.

small discrepancy observed may be attributed to the limited size of our cavity ensemble (12 stirrer configurations) in the full-wave simulation.

Both the stochastic and full-wave simulations were conducted on a workstation with Intel Xeon silver 4114 CPU and 208 GB of memory. Taking the dielectric cube case as an example, the construction of S-DGF IE matrices took 18.4 min, and the solution of the IE matrices was obtained in 12 min. Regarding the full-wave simulations of 12 cavity configurations, each simulation took 7 h and 31 min on average. Thereby a total time of 5412 min is required to obtain the results of the configuration ensemble.

B. Verification of Cavity Q-Factor for Wall Coating

The next numerical experiment is to evaluate the statistics of Q-factor due to the power dissipated in the wall coating. Specifically, we consider an Eccosorb LS-24 absorber with a thickness of $\tau = 5\,\text{mm}$ serving as a wall coating. This thin absorber is applied to a confined area on the PEC wall of a 3-D closed cavity with a volume of $V = 1\,\text{m}^3$. The relative permittivity and permeability of the absorber are $\epsilon_r = 13.7666 - 14.9681j$ and $\mu_r = 1$ at 1 GHz, respectively. The composite Q-factor (Q_{ref}) obtained using the formulation (7.116) in [17] are considered as reference results.

In our proposed approach, we employ simple small electric dipoles with a length of $l = 5\,\text{mm}$ as the cavity excitation and E-field probes. Following the procedure outlined in Section II-I-B, we use 5k GOE random matrices with dimensions of 2000×2000 to generate a statistical ensemble of S-DGF IE matrices. Consequently, a total of 5k Q-factor samples are computed. The average Q-factor ($\langle Q_{\text{wcl}} \rangle$) is obtained by averaging these samples. The results for varying surface coating areas (A) are plotted in Fig. 12, demonstrating a good agreement between the proposed approach and the reference results.

Moreover, Fig. 13 plots the PDFs of the calculated Q-factor concerning the wall coating areas. For each of the probability distributions, we calculate the mean value μ and the standard derivation σ. It is noted that as the coating area increases, the loss mechanism tends toward the distributed case. The statistics of the cavity Q-factor closely resemble a Gaussian distribution $\mathcal{N}(\mu, \sigma)$, as discussed in [24]. In addition, the standard derivation in the Q-factor decreases as the surface coating area increases.

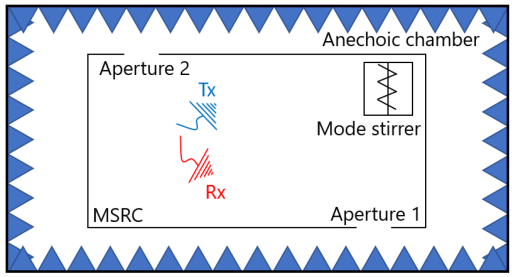

Fig. 14. Illustration of the experiment setup.

C. Validation of Cavity Q-Factor for Aperture Leakage

Finally, we experimentally validate the proposed work for predicting the statistics of Q-factor attributed to the power loss through aperture leakage. The experimental setup is illustrated in Fig. 14. A SMART 800 MSRC is placed inside an anechoic chamber. The dimension of the MSRC is $0.784\,\text{m} \times 1.494\,\text{m} \times 1\,\text{m}$. Two square apertures of dimension $0.3048\,\text{m} \times 0.3048\,\text{m}$ are located on the opposite walls of MSRC. We can open one aperture at a time to examine the effects of power loss, as depicted in Fig. 15(a). The Tx and receiver are implemented using two monocone antennas, as shown in Fig. 15(b). The configuration ensemble is generated by rotating a paddle wheel acting as the mechanical mode stirrer.

We first perform the S-parameter measurement with both apertures closed. The stirrer is rotated 100 positions over 360°. At each stir state, S-parameters of Tx and Rx antennas, S_{11} and S_{21}, are measured and recorded from 1 to 1.25 GHz with 0.025 MHz frequency stepping. To avoid measurements at multiple locations to calculate cavity energy density, we utilize the ensemble average over the stirrer states. The frequency-dependent Q-factor is obtained by [45], [46]

$$Q_{\text{o}}(f) = \frac{16\pi^2 V}{\eta_{\text{TX}}\eta_{\text{RX}}\lambda^3} \left\langle \frac{|S_{21}(f)|^2}{1 - |S_{11}(f)|^2} \right\rangle_{\text{stirr}} \tag{66}$$

where V is the volume of MSRC, η_{TX} and η_{RX} are the Tx and Rx antenna efficiencies. A total number of 10 001 Q-factor

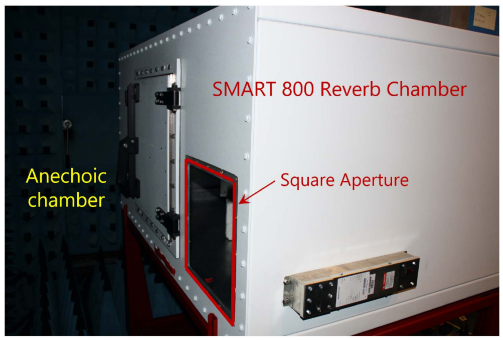

(a)

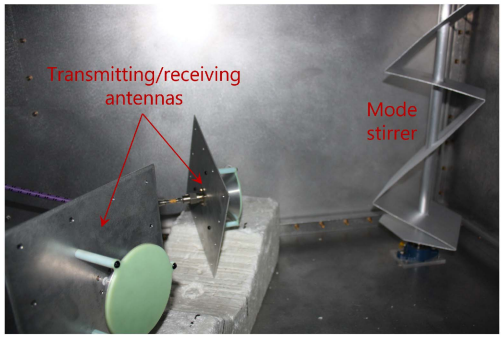

(b)

Fig. 15. Configuration of the MSRC testing environment. (a) Exterior view. (b) Interior view.

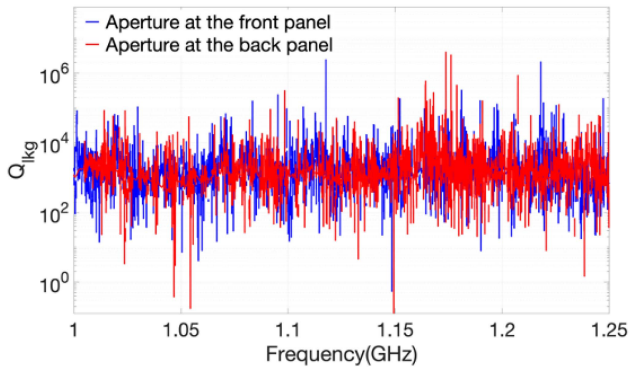

Fig. 16. Measurement result of Q-factor and Q_{lkg}.

samples are obtained from 1 to 1.25 GHz. We then perform the measurement with the same experimental setting while opening the aperture at the front panel of the MSRC. The resulting cavity Q-factor is denoted by Q_{t}. Therefore, the Q-factor due to the aperture leakage Q_{lkg} can be recovered by

$$Q_{\mathrm{lkg}} = 1/\left(1/Q_{\mathrm{t}} - 1/Q_{\mathrm{o}}\right). \tag{67}$$

Finally, we repeat the experiment by opening the aperture on the back panel of the MSRC. Thereby, two sets of measurement data (denoted by front panel and back panel) for Q_{lkg} are obtained. As depicted in Fig. 16, quasi-random fluctuations between frequencies are observed due to the stochastic nature of the cavity field.

The objective of this study is to predict the probability distribution of Q_{lkg} within the frequency range 1–1.25 GHz. To

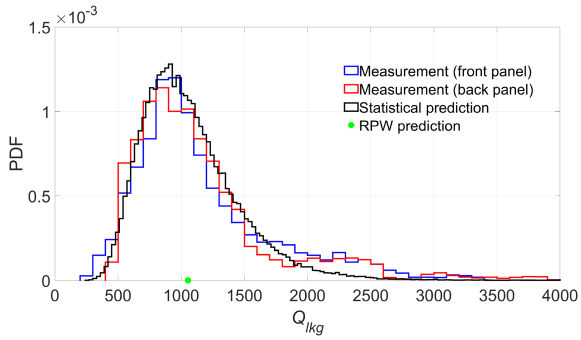

Fig. 17. PDF of the cavity Q-factor for aperture leakage.

achieve this, we divide the range into five frequency bands, each with bandwidth 50 MHz. Our proposed procedure, detailed in Section III-A, is then applied at frequencies ranging from 1 to 1.25 GHz with increments of 0.05 GHz. At each frequency point, we employ 10 k GOE random matrices to generate an ensemble of S-DGF IE matrices in (61). Therefore, a total of 60 k Q-factor samples are computed with the proposed work. Moreover, we have used the RPW method at these frequency points and computed the mean value of the cavity Q-factor. The results are illustrated in Fig. 17. We notice that the prediction from the proposed work shows a good agreement with the measurement results.

VI. Conclusion

This article aims to address an open question about the statistical characterization of cavity Q-factor caused by localized losses, such as aperture leakage and absorptive loading. A novel hybrid deterministic-stochastic computing model is proposed that integrates component-specific (loading) and site-specific (aperture) features with the statistical representation of complex cavity environments. Experimental results are supplied to validate the proposed work.

The research findings hold significant practical applications in the power balance method [20], [47] for characterizing the response of a complex EM system to a high-frequency external excitation, in which the cavity Q-factor is one of the most important input parameters. Given that the proposed work provides a statistical cavity Q-factor, a natural extension is to develop a statistical power balance model to analyze the stochastic power flow in complex systems. Moreover, leveraging the calculated cavity Q-factor, the applications extend to the computation of the energy decay factor, the analysis of the power delay profile, and the control of the coherence bandwidth in the wireless OTA testing in loaded reverberation chambers [48].

Appendix

A. Covariance of Eigenvectors in $\overline{\mathbf{G}}_{\mathrm{S}}^{mm}$

As illustrated in Fig. 2, the covariance function of transverse vector components can be calculated by

$$\left\langle \Psi_i^{\mathrm{m},x}\left(\mathbf{r}\right), \Psi_i^{\mathrm{m}}, x\left(\mathbf{r}'\right)\right\rangle$$

$$
\begin{aligned}
&= \frac{2}{V}\Big\langle (\cos\psi_n\cos\phi_n\cos\theta_n - \sin\psi_n\sin\phi_n)^2 \\
&\cos\left(k_i\hat{\mathbf{e}}_n\cdot\mathbf{r}+\beta_n\right)\cos\left(k_i\hat{\mathbf{e}}_n\cdot\mathbf{r}'+\beta_n\right)\Big\rangle \\
&= \frac{1}{V}\big\langle\big(\cos^2\psi_n\cos^2\phi_n\cos^2\theta_n - 2\cos\theta_n\cos\psi_n\cos\phi_n\sin\psi_n\sin\phi_n \\
&+ \sin^2\psi_n\sin^2\phi_n\big)\left[\cos(k_i\hat{\mathbf{e}}_n\cdot\hat{\mathbf{z}}R)+\cos(k_i\hat{\mathbf{e}}_n\cdot(\mathbf{r}+\mathbf{r}')+2\beta_n)\right]\big\rangle \\
&= \frac{1}{V}\frac{1}{2}\int_0^{\pi}\left[\frac{1}{2}\times\frac{1}{2}\cos^2\theta_n+\frac{1}{2}\times\frac{1}{2}\right]\cos\left(k_iR\cos\theta_n\right)\sin\theta_n d\theta_n \\
&= \frac{1}{8V}\int_{-1}^{1}\left(u^2+1\right)\cos\left(k_iRu\right)du \\
&= \frac{1}{2V}\left[\frac{\sin k_iR}{k_iR}-\frac{\sin k_iR - k_iR\cos k_iR}{k_i^3R^3}\right] \\
&= \frac{1}{3V}f_{\perp}\left(k_iR\right).
\end{aligned}
$$

Similarly, we could also derive the other two covariance functions

$$
\begin{aligned}
\left\langle\Psi_i^{\mathrm{m},y}(\mathbf{r}),\Psi_i^{\mathrm{m},y}(\mathbf{r}')\right\rangle &= \frac{1}{2V}\left[\frac{\sin k_iR}{k_iR}-\frac{\sin k_iR - k_iR\cos k_iR}{(k_iR)^3}\right] \\
&= \frac{1}{3V}f_{\perp}\left(k_iR\right) \\
\left\langle\Psi_i^{\mathrm{m},z}(\mathbf{r}),\Psi_i^{\mathrm{m},z}(\mathbf{r}')\right\rangle &= \frac{1}{V}\frac{\sin k_iR - k_iR\cos k_iR}{(k_iR)^3} \\
&= \frac{1}{3V}f_{//}\left(k_iR\right).
\end{aligned}
$$

B. Covariance of Eigenvectors in $\overline{\mathbf{G}}_{\mathrm{S}}^{me}$

Substituting (16) and (14) into $\mathcal{C}_{xy}^{\mathrm{me}}(R)$, we can obtain

$$
\begin{aligned}
&\left\langle\Psi_i^{\mathrm{m},x}(\mathbf{r}),\Psi_i^{\mathrm{e},y}(\mathbf{r}')\right\rangle \\
&= \frac{2}{V}\Big\langle(\cos\psi_n\cos\phi_n\cos\theta_n-\sin\psi_n\sin\phi_n)(-\sin\psi_n\sin\phi_n\cos\theta_n \\
&+\cos\psi_n\cos\phi_n)\sin\left(k_i\hat{\mathbf{e}}_n\cdot\mathbf{r}+\beta_n\right)\cos\left(k_i\hat{\mathbf{e}}_n\cdot\mathbf{r}'+\beta_n\right)\Big\rangle \\
&= \frac{1}{V}\big\langle\big(-\cos\psi_n\cos\phi_n\sin\psi_n\sin\phi_n\cos^2\theta_n+\cos\theta_n\big(\cos^2\psi_n \\
&\times\cos^2\phi_n+\sin^2\psi_n\sin^2\phi_n\big)-\cos\psi_n\cos\phi_n\sin\psi_n\sin\phi_n\big) \\
&\left[\sin\left(k_i\hat{\mathbf{e}}_n\cdot\hat{\mathbf{z}}R\right)+\sin\left(k_i\hat{\mathbf{e}}_n\cdot(\mathbf{r}+\mathbf{r}')+2\beta_n\right)\right]\big\rangle \\
&= \frac{1}{V}\frac{1}{2}\int_0^{\pi}\left[\left(\frac{1}{2}\times\frac{1}{2}+\frac{1}{2}\times\frac{1}{2}\right)\cos\theta_n\right]\sin\left(k_iR\cos\theta_n\right)\sin\theta_n d\theta_n \\
&= \frac{1}{4V}\int_{-1}^{1}u\sin\left(k_iRu\right)du \\
&= \frac{1}{2V}\frac{\sin k_iR - k_iR\cos k_iR}{(k_iR)^2} \\
&= \frac{k_iR}{6V}f_{//}\left(k_iR\right).
\end{aligned}
$$

Similarly, we could also have

$$
\begin{aligned}
\left\langle\Psi_i^{\mathrm{m},y}(\mathbf{r}),\Psi_i^{\mathrm{e},x}(\mathbf{r}')\right\rangle &= -\frac{1}{2V}\frac{\sin k_iR - k_iR\cos k_iR}{(k_iR)^2} \\
&= -\frac{k_iR}{6V}f_{//}\left(k_iR\right)
\end{aligned}
$$

and all the other elements in the covariance matrix are zero.

C. Finite-Dimensional Discretization of SIE Matrices for Electric Dipole Case

Let us start with the general expression of the impedance matrix $\mathbf{Z}_{\mathrm{S}}$ described as

$$
\mathbf{Z}_{\mathrm{S}} = \begin{bmatrix} \mathrm{Z}_{\mathrm{S}}^{\mathrm{t,t}} & \mathrm{Z}_{\mathrm{S}}^{\mathrm{t,r}} \\ \mathrm{Z}_{\mathrm{S}}^{\mathrm{r,t}} & \mathrm{Z}_{\mathrm{S}}^{\mathrm{r,r}} \end{bmatrix} = j\omega\mu\int\mathbf{v}(\mathbf{r})\cdot\int\overline{\mathbf{G}}_0^{\mathrm{ee}}(\mathbf{r},\mathbf{r}')\cdot\mathbf{v}(\mathbf{r}')d\mathbf{r}'d\mathbf{r}. \tag{68}
$$

Obviously, $\mathrm{Z}_{\mathrm{S}} = \mathrm{Z}_{\mathrm{S}}^{\mathrm{r,r}}$ and $\mathrm{C}_{\mathrm{S}} = -\mathrm{Z}_{\mathrm{S}}^{\mathrm{r,t}}$ will satisfy (40) and (41), respectively. Substituting (7) into (68), we have

$$
\mathbf{Z}_{\mathrm{S}} = j\omega\mu\int\mathbf{v}(\mathbf{r})\cdot\int\mathrm{Re}\left[\overline{\mathbf{G}}_0^{\mathrm{ee}}(\mathbf{r},\mathbf{r}')\right]\cdot\mathbf{v}(\mathbf{r}')d\mathbf{r}'d\mathbf{r} \tag{69}
$$

$$
+ j\omega\mu\int\mathbf{v}(\mathbf{r})\cdot\int\sum_m\frac{\overline{\mathbf{D}}_{\mathrm{S}}^{\mathrm{ee}}(\mathbf{r},\mathbf{r}';k_m)}{\tilde{\lambda}_m-j\alpha}\frac{kV}{2\pi^2}\cdot\mathbf{v}(\mathbf{r}')d\mathbf{r}'d\mathbf{r}. \tag{70}
$$

Accordingly, the impedance matrix $\mathbf{Z}_{\mathrm{S}}$ consists of two part. The first part gives us

$$
j\omega\mu\int\mathbf{v}(\mathbf{r})\cdot\int\mathrm{Re}\left[\overline{\mathbf{G}}_0^{\mathrm{ee}}(\mathbf{r},\mathbf{r}')\right]\cdot\mathbf{v}(\mathbf{r}')d\mathbf{r}'d\mathbf{r} = j\mathbf{X}_0.
$$

For the second part, we first consider the outer product in the numerator

$$
\begin{aligned}
&\int\mathbf{v}(\mathbf{r})\cdot\int\overline{\mathbf{D}}_{\mathrm{S}}^{\mathrm{ee}}(\mathbf{r},\mathbf{r}';k_m)\cdot\mathbf{v}(\mathbf{r}')d\mathbf{r}'d\mathbf{r} \\
&= \int\mathbf{v}(\mathbf{r})\cdot\int\left(\mathbf{\Psi}_i^{\mathrm{e}}(\mathbf{r},k_i)\otimes\mathbf{\Psi}_i^{\mathrm{e}}(\mathbf{r}',k_i)\right)\cdot\mathbf{v}(\mathbf{r}')d\mathbf{r}'d\mathbf{r} \\
&= \iint\left[\mathbf{v}(\mathbf{r})\cdot\mathbf{\Psi}_i^{\mathrm{e}}(\mathbf{r},k_i)\right]\left[\mathbf{\Psi}_i^{\mathrm{e}}(\mathbf{r}',k_i)\cdot\mathbf{v}(\mathbf{r}')\right]d\mathbf{r}'d\mathbf{r}.
\end{aligned} \tag{71}
$$

Based on the property of RWM approximation, it is easy to show that both $[\mathbf{v}(\mathbf{r})\cdot\mathbf{\Psi}_i^{\mathrm{e}}(\mathbf{r},k_i)]$ and $[\mathbf{\Psi}_i^{\mathrm{e}}(\mathbf{r}',k_i)\cdot\mathbf{v}(\mathbf{r}')]$ follow Gaussian distribution. After multiplying the remaining coefficient $j\omega\mu\frac{kV}{2\pi^2}$ in (70), the matrix entries in (71) are the results of the product of Gaussian random variables, whose covariance between trial and testing triangle function is expressed by

$$
\begin{aligned}
&\left\langle j\omega\mu\int\mathbf{v}(\mathbf{r})\cdot\left[\int\overline{\mathbf{D}}_{\mathrm{S}}^{\mathrm{ee}}(\mathbf{r},\mathbf{r}';k_m)\frac{kV}{2\pi^2}\cdot\mathbf{v}(\mathbf{r}')\right]d\mathbf{r}'d\mathbf{r}\right\rangle \\
&= j\omega\mu\int\mathbf{v}(\mathbf{r})\cdot\int\left\langle\overline{\mathbf{D}}_{\mathrm{S}}^{\mathrm{ee}}(\mathbf{r},\mathbf{r}';k_m)\right\rangle\frac{kV}{2\pi^2}\cdot\mathbf{v}(\mathbf{r}')d\mathbf{r}'d\mathbf{r} \\
&\approx j\omega\mu\iint\mathbf{v}(\mathbf{r})\cdot\left(-\frac{1}{\pi}\mathrm{Im}\left[\overline{\overline{\mathbf{G}}}_0(\mathbf{r},\mathbf{r}';k)\right]\cdot\mathbf{v}(\mathbf{r}')\right)d\mathbf{r}'d\mathbf{r} \\
&= \frac{j}{\pi}\mathbf{R}_0.
\end{aligned}
$$

In the abovementioned derivation, we have used the result of (8) and the fact of $k_m \approx k$. Then, the correlated Gaussian random variables associated with individual triangle functions can be constructed using the discrete Karhunen–Loeve expansion

$$[\tilde{\boldsymbol{w}}_m] = \sqrt{\mathbf{R}_0}\,[\boldsymbol{w}_m].$$

Therefore, the impedance matrix $\mathbf{Z}_{\rm S}$ is written as

$$\mathbf{Z}_{\rm S} = j\mathbf{X}_0 + \frac{j}{\pi}\sum_m \frac{\tilde{\boldsymbol{w}}_m \tilde{\boldsymbol{w}}_m^T}{\tilde{\lambda}_m - j\alpha}.$$

In the diffusive case

$$\begin{bmatrix} \mathrm{Z}_{\rm S}^{\rm t,t} & \mathrm{Z}_{\rm S}^{\rm t,r} \\ \mathrm{Z}_{\rm S}^{\rm r,t} & \mathrm{Z}_{\rm S}^{\rm r,r} \end{bmatrix} = j\begin{bmatrix} \mathrm{X}_0^{\rm t} & 0 \\ 0 & \mathrm{X}_0^{\rm r} \end{bmatrix} + \frac{j}{\pi}\sum_m \left\{ \sqrt{\begin{bmatrix} \mathrm{R}_0^{\rm t} & 0 \\ 0 & \mathrm{R}_0^{\rm r} \end{bmatrix}} \begin{bmatrix} w_m^{\rm t} \\ w_m^{\rm r} \end{bmatrix} \cdot \frac{1}{\tilde{\lambda}_m - j\alpha} \cdot \begin{bmatrix} w_m^{\rm t} & w_m^{\rm r} \end{bmatrix} \sqrt{\begin{bmatrix} \mathrm{R}_0^{\rm t} & 0 \\ 0 & \mathrm{R}_0^{\rm r} \end{bmatrix}} \right\}.$$

Thus, we have the explicit form of $\mathrm{Z}_{\rm S}$ and $\mathrm{C}_{\rm S}$ as

$$\mathrm{Z}_{\rm S} = j\mathrm{X}_0^{\rm r} + \frac{j}{\pi}\sum_m \sqrt{\mathrm{R}_0^{\rm r}} \cdot \frac{(w_m^{\rm r})^2}{\tilde{\lambda}_m - j\alpha} \cdot \sqrt{\mathrm{R}_0^{\rm r}}$$

$$\mathrm{C}_{\rm S} = -\frac{j}{\pi}\sum_m \sqrt{\mathrm{R}_0^{\rm r}} \cdot \frac{w_m^{\rm r} w_m^{\rm t}}{\tilde{\lambda}_m - j\alpha} \cdot \sqrt{\mathrm{R}_0^{\rm t}}.$$

D. Finite-Dimensional Discretization of SIE Matrices for Dielectric Loading Case

In (47), we first have the impedance matrices for the dielectric medium

$$\mathbf{Z}_{\rm H}^{\rm e,j} = j\omega\mu \iiint\!\!\iint \mathbf{v}(\mathbf{r}) \cdot \left[\pi_\tau\left(\overline{\mathbf{G}}_{\rm H}^{\rm ee}(\mathbf{r},\mathbf{r}')\right) \cdot \mathbf{v}(\mathbf{r}')\right] dS' dS \quad (72)$$

$$\mathbf{Z}_{\rm H}^{\rm e,m} = \iiint\!\!\iint \mathbf{v}(\mathbf{r}) \cdot \left[\pi_\tau\left(\overline{\mathbf{G}}_{\rm H}^{\rm em}(\mathbf{r},\mathbf{r}')\right) \cdot \mathbf{v}(\mathbf{r}')\right] dS' dS \quad (73)$$

$$\mathbf{Z}_{\rm H}^{\rm h,j} = \iiint\!\!\iint \mathbf{v}(\mathbf{r}) \cdot \left[\pi_\tau\left(\overline{\mathbf{G}}_{\rm H}^{\rm me}(\mathbf{r},\mathbf{r}')\right) \cdot \mathbf{v}(\mathbf{r}')\right] dS' dS \quad (74)$$

$$\mathbf{Z}_{\rm H}^{\rm h,m} = j\omega\epsilon \iiint\!\!\iint \mathbf{v}(\mathbf{r}) \cdot \left[\pi_\tau\left(\overline{\mathbf{G}}_{\rm H}^{\rm mm}(\mathbf{r},\mathbf{r}')\right) \cdot \mathbf{v}(\mathbf{r}')\right] dS' dS. \quad (75)$$

For the impedance matrices using the stochastic DGF, we have

$$\mathbf{Z}_{\rm S}^{\rm e,j} = j\omega\mu \iiint\!\!\iint \mathbf{v}(\mathbf{r}) \cdot \left[\pi_\tau\left(\overline{\mathbf{G}}_{\rm S}^{\rm ee}(\mathbf{r},\mathbf{r}')\right) \cdot \mathbf{v}(\mathbf{r}')\right] dS' dS \quad (76)$$

$$\mathbf{Z}_{\rm S}^{\rm e,m} = \iiint\!\!\iint \mathbf{v}(\mathbf{r}) \cdot \left[\pi_\tau\left(\overline{\mathbf{G}}_{\rm S}^{\rm em}(\mathbf{r},\mathbf{r}')\right) \cdot \mathbf{v}(\mathbf{r}')\right] dS' dS \quad (77)$$

$$\mathbf{Z}_{\rm S}^{\rm h,j} = \iiint\!\!\iint \mathbf{v}(\mathbf{r}) \cdot \left[\pi_\tau\left(\overline{\mathbf{G}}_{\rm S}^{\rm me}(\mathbf{r},\mathbf{r}')\right) \cdot \mathbf{v}(\mathbf{r}')\right] dS' dS \quad (78)$$

$$\mathbf{Z}_{\rm S}^{\rm h,m} = j\omega\epsilon \iiint\!\!\iint \mathbf{v}(\mathbf{r}) \cdot \left[\pi_\tau\left(\overline{\mathbf{G}}_{\rm S}^{\rm mm}(\mathbf{r},\mathbf{r}')\right) \cdot \mathbf{v}(\mathbf{r}')\right] dS' dS. \quad (79)$$

Following the similar procedure of the derivation in Appendix C, we can derive

$$\mathbf{Z}_{\rm S}^{\rm e,j} = j\mathbf{X}_0^{\rm e,j} + \frac{j}{\pi}\sum_m \frac{\tilde{\boldsymbol{w}}_m^{\rm e}(\tilde{\boldsymbol{w}}_m^{\rm e})^T}{\tilde{\lambda}_m - j\alpha} \quad (80)$$

$$\mathbf{Z}_{\rm S}^{\rm e,m} = \mathbf{R}_0^{\rm e,m} - \frac{1}{\pi}\sum_m \frac{\tilde{\boldsymbol{w}}_m^{\rm e}(\tilde{\boldsymbol{w}}_m^{\rm m})^T}{\tilde{\lambda}_m - j\alpha} \quad (81)$$

$$\mathbf{Z}_{\rm S}^{\rm h,j} = \mathbf{R}_0^{\rm h,j} - \frac{1}{\pi}\sum_m \frac{\tilde{\boldsymbol{w}}_m^{\rm m}(\tilde{\boldsymbol{w}}_m^{\rm e})^T}{\tilde{\lambda}_m - j\alpha} \quad (82)$$

$$\mathbf{Z}_{\rm S}^{\rm h,m} = j\mathbf{X}_0^{\rm h,m} + \frac{j}{\pi}\sum_m \frac{\tilde{\boldsymbol{w}}_m^{\rm m}(\tilde{\boldsymbol{w}}_m^{\rm m})^T}{\tilde{\lambda}_m - j\alpha}. \quad (83)$$

Thus, combining (80)–(83), we have the final expression of the impedance matrix for dielectric loading as

$$\begin{bmatrix} \mathbf{Z}_{\rm S}^{\rm e,j} & \mathbf{Z}_{\rm S}^{\rm e,m} \\ \mathbf{Z}_{\rm S}^{\rm h,j} & \mathbf{Z}_{\rm S}^{\rm h,m} \end{bmatrix} = \begin{bmatrix} j\mathbf{X}_0^{\rm e,j} & \mathbf{R}_0^{\rm e,m} \\ \mathbf{R}_0^{\rm h,j} & j\mathbf{X}_0^{\rm h,m} \end{bmatrix} + \frac{j}{\pi}\sum_m \frac{\tilde{\boldsymbol{w}}_m \tilde{\boldsymbol{w}}_m^T}{\tilde{\lambda}_m - j\alpha} \quad (84)$$

where $\tilde{\boldsymbol{w}}_m$ are correlated Gaussian random variables associated with individual RWG functions, which can be constructed using the discrete Karhunen–Loeve expansion

$$[\tilde{\boldsymbol{w}}_m] = \begin{bmatrix} \mathbf{R}_0^{\rm e,j} & j\mathbf{X}_0^{\rm e,m} \\ j\mathbf{X}_0^{\rm h,j} & \mathbf{R}_0^{\rm h,m} \end{bmatrix}^{1/2} \begin{bmatrix} \boldsymbol{w}_m^{\rm e} \\ \boldsymbol{w}_m^{\rm m} \end{bmatrix}.$$

And $\boldsymbol{w}_m^{\rm e}$ and $\boldsymbol{w}_m^{\rm m}$ are zero mean, unit variance independent Gaussian random variables.

ACKNOWLEDGMENT

The authors would like to thank Dr. Luk Arnaut at Queen Mary University of London for valuable discussions on the cavity quality factor and stochastic Green's function. The authors also would like to thank all valuable comments and suggestions from anonymous reviewers, which helped to improve the quality of this article.

REFERENCES

[1] D. Hill, "Electronic mode stirring for reverberation chambers," *IEEE Trans. Electromagn. Compat.*, vol. 36, no. 4, pp. 294–299, Nov. 1994.
[2] L. Cappetta, M. Feo, V. Fiumara, V. Pierro, and M. Pinto, "Electromagnetic chaos in mode-stirred reverberation enclosures," *IEEE Trans. Electromagn. Compat.*, vol. 40, no. 3, pp. 185–192, Aug. 1998.
[3] V. Rajamani, C. F. Bunting, and J. C. West, "Stirred-mode operation of reverberation chambers for EMC testing," *IEEE Trans. Instrum. Meas.*, vol. 61, no. 10, pp. 2759–2764, Oct. 2012.
[4] L. Arnaut, "Mode-stirred reverberation chambers: A paradigm for spatio-temporal complexity in dynamic electromagnetic environments," *Wave Motion*, vol. 51, no. 4, pp. 673–684, 2014.
[5] J. C. West, R. Bakore, and C. F. Bunting, "Statistics of the current induced within a partially shielded enclosure in a reverberation chamber," *IEEE Trans. Electromagn. Compat.*, vol. 59, no. 6, pp. 2014–2022, Dec. 2017.
[6] C. Bunting and S.-P. Yu, "Field penetration in a rectangular box using numerical techniques: An effort to obtain statistical shielding effectiveness," *IEEE Trans. Electromagn. Compat.*, vol. 46, no. 2, pp. 160–168, May 2004.
[7] R. Holland and R. St John, "Statistical response of EM-driven cables inside an overmoded enclosure," *IEEE Trans. Electromagn. Compat.*, vol. 40, no. 4, pp. 311–324, Nov. 1998.
[8] D. Fedeli, G. Gradoni, V. M. Primiani, and F. Moglie, "Accurate analysis of reverberation field penetration into an equipment-level enclosure," *IEEE Trans. Electromagn. Compat.*, vol. 51, no. 2, pp. 170–180, May 2009.
[9] S. Hemmady, T. Antonsen, E. Ott, and S. Anlage, "Statistical prediction and measurement of induced voltages on components within complicated enclosures: A wave-chaotic approach," *IEEE Trans. Electromagn. Compat.*, vol. 54, no. 4, pp. 758–771, Aug. 2012.
[10] Z. B. Drikas et al. Gil,, "Application of the random coupling model to electromagnetic statistics in complex enclosures," *IEEE Trans. Electromagn. Compat.*, vol. 56, no. 6, pp. 1480–1487, Dec. 2014.

[11] G. Gradoni, T. M. Antonsen, and E. Ott, "Random coupling model for the radiation of irregular apertures," *Radio Sci.*, vol. 50, no. 7, pp. 678–687, 2015.
[12] M. Mehri and N. Masoumi, "Statistical prediction and quantification of radiated susceptibility for electronic systems PCB in electromagnetic polluted environments," *IEEE Trans. Electromagn. Compat.*, vol. 59, pp. 498–508, Apr. 2017.
[13] P. Kildal and K. Rosengren, "Correlation and capacity of MIMO systems and mutual coupling, radiation efficiency, and diversity gain of their antennas: Simulations and measurements in a reverberation chamber," *IEEE Commun. Mag.*, vol. 42, pp. 104–112, Dec. 2004.
[14] J. D. Sanchez-Heredia, J. F. Valenzuela-Valdes, A. M. Martinez-Gonzalez, and D. A. Sanchez-Hernandez, "Emulation of MIMO Rician-fading environments with mode-stirred reverberation chambers," *IEEE Trans. Antennas Propag.*, vol. 59, no. 2, pp. 654–660, Feb. 2011.
[15] A. Marin-Soler et al., "Sample selection algorithms for enhanced MIMO antenna measurements using mode-stirred reverberation chambers," *IEEE Trans. Antennas Propag.*, vol. 60, no. 8, pp. 3892–3900, Aug. 2012.
[16] K. A. Remley et al., "Configuring and verifying reverberation chambers for testing cellular wireless devices," *IEEE Trans. Electromagn. Compat.*, vol. 58, no. 3, pp. 661–672, Jun. 2016.
[17] D. A. Hill, *Electromagnetic Fields in Cavities: Deterministic and Statistical Theories*. Hoboken, NJ, USA: Wiley, 2009.
[18] P. G. Bremner, D. Trout, G. Vazquaz, N. Nourshamsi, J. C. West, and C. F. Bunting, "Modal Q factor and modal overlap of electrically small avionics boxes," in *Proc. IEEE Symp. Electromagn. Compatibility, Signal Integrity Power Integrity*, 2018, pp. 286–291.
[19] P. Corona, G. Latmiral, and E. Paolini, "Performance and analysis of a reverberating enclosure with variable geometry," *IEEE Trans. Electromagn. Compat.*, vol. EMC- 22, no. 1, pp. 2–5, Jan. 1980.
[20] D. A. Hill, M. T. Ma, A. R. Ondrejka, B. F. Riddle, M. L. Crawford, and R. T. Johnk, "Aperture excitation of electrically large, lossy cavities," *IEEE Trans. Electromagn. Compat.*, vol. 36, pp. 169–178, Aug. 1994.
[21] L. R. Arnaut and G. Gradoni, "Probability distribution of the quality factor of a mode-stirred reverberation chamber," *IEEE Trans. Electromagn. Compat.*, vol. 55, no. 1, pp. 35–44, Jan. 2013.
[22] Arnaut R. Luk, Andries I. Mihai, Jérôme Sol, and P. Besnier, "Evaluation method for the probability distribution of the quality factor of mode-stirred reverberation chambers," *IEEE Trans. Antennas Propag.*, vol. 62, no. 8, pp. 4199–4208, Aug. 2014.
[23] L. R. Arnaut, P. Besnier, J. Sol, and M. I. Andries, "On the uncertainty quantification of the quality factor of reverberation chambers," *IEEE Trans. Electromagn. Compat.*, vol. 61, no. 3, pp. 823–832, Mar. 2019.
[24] A. Gifuni, G. Ferrara, M. Migliaccio, and A. Sorrentino, "Estimate of the probability density function of the quality factor of mode tuned, source stirred and mode stirred reverberation chambers," *IEEE Trans. Electromagn. Compat.*, vol. 57, no. 5, pp. 926–936, May 2015.
[25] G. Ferrara, A. Gifuni, M. Migliaccio, and A. Sorrentino, "Probability density function for the quality factor of vibrating reverberation chambers," in *Proc. IEEE Metrol. Aerosp.*, 2015, pp. 230–234.
[26] A. Gifuni, "Probability density function of the quality factor for reverberation chambers operating with hybrid stirring including frequency stirring," *IEEE Trans. Electromagn. Compat.*, vol. 58, no. 3, pp. 919–922, Mar. 2016.
[27] S. Lin, Z. Peng, and T. M. Antonsen, "A stochastic Green's function for solution of wave propagation in wave-chaotic environments," *IEEE Trans. Antennas Propag.*, vol. 68, no. 5, pp. 3919–3933, May 2020.
[28] S. Lin, Y. Shao, and Z. Peng, "On the vectorial property of stochastic dyadic Green's function in complex electronic enclosures," in *Proc. IEEE Int. Symp. Electromagn. Compat. Signal/Power Integrity*, 2022, pp. 350–355.
[29] S. Lin et al., "Predicting statistical wave physics in complex enclosures: A. stochastic dyadic Green's function approach," *IEEE Trans. Electromagn. Compat.*, vol. 65, no. 2, pp. 436–453, Feb. 2023.
[30] S. Lin, Y. Shao, Z. Peng, B. D. Addissie, and Z. B. Drikas, "Statistical characterization of cavity quality factor via the stochastic Green's function approach," in *Proc. IEEE Symp. Electromagn. Compat. Signal/Power Integrity*, 2023, pp. 183–188.
[31] E. Ott and W. M. Manheimer, "Cavity Q for ergodic eigenmodes," *Phys. Rev. A*, vol. 25, pp. 1808–1810, Mar. 1982.
[32] M. V. Berry, "Regular and irregular semiclassical wavefunctions," *J. Phys. A: Math. Gen.*, vol. 10, no. 12, 1977, Art. no. 2083.
[33] E. Wigner, "Random matrices in physics," *SIAM Rev.*, vol. 9, no. 1, pp. 1–23, 1967.
[34] J. G. V. Bladel, *Electromagnetic Fields*. Piscataway, NJ, USA: IEEE Press, 2007, ch. 10, pp. 509–561.
[35] Y. Chien and K.-S. Fu, "On the generalized Karhunen-Loeve expansion (corresp.)," *IEEE Trans. Inf. Theory*, vol. 13, no. 3, pp. 518–520, Jul. 1967.
[36] A. Papoulis and S. U. Pillai, *Probability, Random Variables, and Stochastic Processes*, 4 ed. New York, NY, USA: McGraw-Hill, 2002.
[37] K. R. Umashankar, A. Taflove, and S. M. Rao, "Electromagnetic scattering by arbitrary shaped three-dimensional homogeneous lossy dielectric objects," *IEEE Trans. Antennas Propagat.*, vol. 34, no. 6, pp. 758–766, Jun. 1986.
[38] S. M. Rao, D. R. Wilton, and A. W. Glisson, "Electromagnetic scattering by surfaces of arbitrary shape," *IEEE Trans. Antennas Propagat.*, vol. AP-30, no. 3, pp. 409–418, May 1982.
[39] Z. Peng, Y. Shao, H. Gao, S. Wang, and S. Lin, "High-fidelity, high-performance computational algorithms for intrasystem electromagnetic interference analysis of IC and electronics," *IEEE Trans. Compon. Packag. Manuf. Technol.*, vol. 7, no. 5, pp. 653–668, May 2017.
[40] R. F. Harrington and J. R. Mautz, "Electromagnetic coupling through apertures by the generalized admittance approach," *Comput. Phys. Commun.*, vol. 68, no. 1, pp. 19–42, 1991.
[41] H. Ling, R. C. Chou, and S. W. Lee, "Shooting and bouncing rays calculating RCS of an arbitrarily shaped cavity," *IEEE Trans. Antennas Propagat.*, vol. 37, no. 2, pp. 194–205, Feb. 1989.
[42] D. A. Hill, "Plane wave integral representation for fields in reverberation chambers," *IEEE Trans. Electromagn. Compat.*, vol. 40, no. 3, pp. 209–217, Aug. 1998.
[43] G. Gradoni, D. Micheli, F. Moglie, and V. M. Primiani, "Absorbing cross section in reverberation chamber: Experimental and numerical results," *Prog. In Electromagn. Res. B*, vol. 45, pp. 187–202, 2012.
[44] S. Kullback and R. A. Leibler, "On information and sufficiency," *Ann. Math. Statist.*, vol. 22, no. 1, pp. 79–86, 1951.
[45] M. Magdowski, B. R. Banjade, and R. Vick, "Measurement of the coupling to shielded cables above a ground plane in a reverberation chamber," in *Proc. Int. Symp. Electromagn. Compat.*, 2016, pp. 234–239.
[46] N. Wellander, M. Elfsberg, and T. Hurtig, "Finding frequencies of enhanced electromagnetic coupling to electronic devices by the use of mode stirred reverberation chambers," in *Proc. Int. Symp. Electromagn. Compat.*, 2017, pp. 1–6.
[47] I. Junqua, J.-P. Parmantier, and F. Issac, "A network formulation of the power balance method for high-frequency coupling," *Electromagnetics*, vol. 25, pp. 603–622, 2005.
[48] X. Chen, P.-S. Kildal, C. Orlenius, and J. Carlsson, "Channel sounding of loaded reverberation chamber for over-the-air testing of wireless devices—coherence bandwidth versus average mode bandwidth and delay spread," *IEEE Antennas Wireless Propag. Lett.*, vol. 8, pp. 678–681, 2009.

Shen Lin (Member, IEEE) received the B.E. degree in optical and electronic information engineering and the M.S. degree in instrument and meter engineering from the Harbin Institute of Technology, Harbin, China, in 2012 and 2014, respectively, and the M.S. degree in optical science and engineering from the University of New Mexico, Albuquerque, NM, USA, in 2019 and the Ph.D. degree in electrical and computer engineering from the University of Illinois at Urbana-Champaign (ECE ILLINOIS), Champaign, IL, USA, in 2022.

He is currently a Postdoctoral Fellow with ECE ILLINOIS. His research interests are in the areas of computational and statistical electromagnetics, including stochastic electromagnetics, quantitative statistical analysis of IC and electronics in complex environments/systems, and nonparametric stochastic algorithms. His research work has an impact on electromagnetic interference and compatibility, signal and power integrity, and wireless communication. The goal is to create a strong bond between classical and quantum electrodynamic physics.

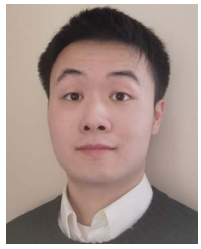

Sangrui Luo (Student Member, IEEE) received the B.S. degree in applied physics from the University of Science and Technology of China, Hefei, China, in 2020. He is currently working toward the Ph.D. degree in electrical engineering with the Department of Electrical and Computer Engineering, University of Illinois at Urbana-Champaign, Champaign, IL, USA.

His research interests include computational electromagnetics and stochastic methods for wave-chaotic problems.

Yang Shao (Member, IEEE) received the B.S. degree in electrical engineering and information science from the University of Science and Technology of China, Hefei, China, in 2003 and the Ph.D. degree in electrical engineering from the Chinese Academy of Sciences, Beijing, China, in 2008.

She was a Postdoctoral Researcher with the ElectroScience Laboratory, Ohio State University, Columbus, OH, USA, in 2009–2014, and a Research Assistant Professor with the Department of Electrical and Computer Engineering, University of New Mexico, Albuquerque, NM, USA, in 2014–2019. She is currently a Teaching Assistant Professor with the Department of Electrical and Computer Engineering, University of Illinois at Urbana-Champaign, Champaign, IL, USA. Her research focuses on electromagnetic compatibility and scientific computing with a particular emphasis on the advancement of computational electromagnetics (EM) and computational thermal analysis. She has primarily been interested in the development of advanced mathematical formulations that may be used in conjunction with powerful numerical solvers to study real-world multiscale structures of integrated circuits, electronics, and antennas. She is also interested in multiphysics engineering application modeling and simulation-aided design, VLSI computer architectures, and multithreading microarchitectures.

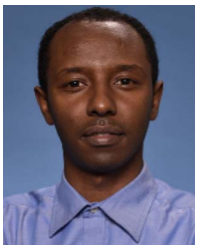

Bisrat D. Addissie received the bachelor's, M.Sc., and Ph.D. degrees in electrical engineering from the University of Maryland, College Park, MD, USA, in 2010, 2015, and 2017, respectively. His Ph.D. dissertation was titled, "Methods for Characterizing Electromagnetic Coupling Statistics in Complex Enclosures."

From 2010 to 2016, he was a Researcher with the U.S. Food and Drug Administration's Electromagnetic Compatibility (EMC) Laboratory where he studied the susceptibility of personal electronic medical devices to nonionizing electromagnetic (EM) emissions from airport security systems. In 2017, he joined the Naval Research Laboratory as an RF Engineer where his research interests include statistical electromagnetics and electromagnetic time-reversal techniques. He has authored and coauthored numerous reports and papers in peer-reviewed journals and conference proceedings.

Dr. Addissie was selected for NRL's Jarome and Isabella Kale Distinguished Scholar Fellowship, in 2019.

Zachary B. Drikas (Member, IEEE) received the B.S. and M.S. degrees in electrical engineering from The George Washington University, Washington, DC, USA, in 2011 and 2012, respectively, and the Ph.D. degree in electrical engineering from Virginia Tech, Blacksburg, VA, USA, in 2020.

He is a Senior Electrical Engineer, with 15 years' experience, with the U.S. Naval Research Laboratory. He is the author or coauthor of 13 peer-reviewed journal articles with 135 citations, and an H-index of 9. He has 30 contributed conference talks. His research and expertise include electromagnetic time-reversal techniques, advanced signal processing techniques, HPM effects on electronics/receiver systems, counter-directed energy (CDEW) applications, ultra-wideband (UWB) radar, and other UWB techniques.

Gabriele Gradoni (Member, IEEE) received the Ph.D. degree in electromagnetics from the Universita' Politecnica delle Marche, Ancona, Italy, in 2010.

He was a Visiting Researcher with the Time, Quantum, and Electromagnetics Team, National Physical Laboratory, Teddington, U.K., in 2008. From 2010 to 2013, he was a Research Associate with the Institute for Research in Electronics and Applied Physics, University of Maryland, College Park, MD, USA. From 2013 to 2016, he was a Research Fellow with the School of Mathematical Sciences, University of Nottingham, U.K., where he was a Full Professor of Mathematics and Electrical Engineering. Since 2023, he has been a Full Professor and Chair of Wireless Communications at the 6G Innovation Centre, Institute for Communication Systems, University of Surrey, Guildford, U.K. Since 2020, he has been an Adjunct Associate Professor with the Department of Electrical and Computer Engineering, University of Illinois at Urbana-Champaign, Champaign, IL, USA. Since 2020, he has been a Royal Society Industry Fellow with British Telecom, U.K. Since 2022, he has been a Visiting Fellow with the Department of Computer Science and Technology, University of Cambridge, Cambridge, U.K. His research interests include probabilistic and asymptotic methods for propagation in complex wave systems, metasurface modeling, quantum/wave chaos, and quantum computational electromagnetics, with applications to electromagnetic compatibility and modern wireless communication systems.

Dr. Gradoni is a member of the Italian Electromagnetics Society. He was the recipient of the URSI Commission B. Young Scientist Award in 2010 and 2016, the Italian Electromagnetics Society Gaetano Latmiral Prize in 2015, and the Honorable Mention IEEE TEMC Richard B. Schulz Transactions Prize Paper Award in 2020. From 2014 to 2021, he was the URSI Commission E. Early Career Representative.

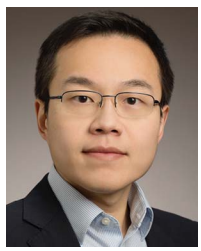

Zhen Peng (Senior Member, IEEE) received the B.S. degree in electrical engineering and information science from the University of Science and Technology of China, Hefei, China, in 2003 and the Ph.D. degree in electromagnetics and microwave engineering from the Chinese Academy of Science, Beijing, China, in 2008.

From 2008 to 2013, he was with the ElectroScience Laboratory, The Ohio State University, Columbus, OH, USA, first as a Postdoctoral Fellow in 2008–2009 and then as a Senior Research Associate in 2010–2013. From 2013 to 2019, he was an Assistant Professor with the Department of Electrical and Computer Engineering, The University of New Mexico (UNM), Albuquerque, NM, USA. He is currently an Associate Professor with the Department of Electrical and Computer Engineering (ECE ILLINOIS), University of Illinois at Urbana-Champaign, Champaign, IL, USA. His research interests are in the area of computational, statistical and applied electromagnetics. The goal is to simulate classical and quantum electrodynamic physics with intelligent algorithms on state-of-the-art computers, where virtual experiments can be performed for the prediction, discovery, and design of complex systems at unprecedented scales. His research work has an impact on both civilian and commercial engineering applications, including advanced antennas, radio frequency integrated circuits, electromagnetic interference and compatibility, signal and power integrity, and wireless communication.

Dr. Peng was the recipient of the 2022 16th European Conference on Antennas and Propagation Best Electromagnetics Paper Award, 2021 30th Conference on Electrical Performance of Electronic Packaging and Systems (EPEPS) Best Conference Paper Award, 2019 IEEE Electromagnetic Compatibility Symposium Best Paper Award, 2019 EPEPS Best Conference Paper Award, 2018 National Science Foundation CAREER Award, 2018 Best Transaction Paper Award—IEEE Transactions on Components, Packaging and Manufacturing Technology, 2017 IEEE Albuquerque Section Outstanding Young Engineer Award, 2016 UNM Electrical and Computer Engineering Department? Distinguished Researcher Award, 2015 Applied Computational Electromagnetics Society Early Career Award, 2014 IEEE Antenna and Propagation Sergei A. Schelkunoff Transactions Prize Paper Award, multiple Young Scientist Awards and the advisor of 12 Best Student Paper Awards to date from various conferences.